Tribology International 189 (2023) 108994

Contents lists available at ScienceDirect

Tribology International

journal homepage: www.elsevier.com/locate/triboint

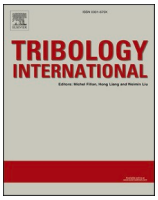

Effect of water temperature and induced acoustic pressure on cavitation erosion behaviour of aluminium alloys

Abhinav Priyadarshi [a,*], Wiktor Krzemień [a], Georges Salloum-Abou-Jaoude [b], James Broughton [a], Koulis Pericleous [c], Dmitry Eskin [d], Iakovos Tzanakis [a,e]

[a] Faculty of Technology, Design and Environment, Oxford Brookes University, Oxford OX33 1HX, United Kingdom
[b] Constellium Technology Center C-TEC, Parc Economique Centr'alp, 725 rue Aristide Bergès, CS10027 Voreppe, France
[c] Computational Science and Engineering Group (CSEG), Department of Mathematics, University of Greenwich, London SE10 9LS, United Kingdom
[d] Brunel Centre for Advance Solidification Technology (BCAST), Brunel University London, Uxbridge UB8 3PH, United Kingdom
[e] Department of Materials, University of Oxford, Oxford OX1 3PH, United Kingdom

ARTICLE INFO

Keywords:
Cavitation erosion
Aluminium cast alloys
Temperature
High-speed imaging
Acoustic pressure

ABSTRACT

Cavitation erosion is a major challenge for marine and fluid machinery systems. This study investigated the erosion performance of two as-cast aluminium alloys exposed to acoustic cavitation in water at temperatures of 10–50 °C and those were then compared with an extruded wrought alloy tested specifically at the temperature of maximum erosion. The results showed that the as-cast A380 alloy displayed exceptional resistance to cavitation erosion, with the lowest mass loss and surface roughness. This finding suggests that the as-cast A380 alloy is a suitable choice for lightweight, high-performance components in applications where cavitation resistance is critical.

1. Introduction

Cavitation (pitting) erosion poses a significant challenge in hydraulic machinery and marine-related equipment, leading to safety risks, service interruptions, and economic losses due to material degradation. Previous studies have highlighted the substantial damage caused by cavitation erosion, with turbine blades experiencing pitting depths of up to 10 mm per year [1]. Under extreme environment, hydroturbine blades can suffer pitting depths exceeding 40 mm, resulting in a metal loss rate of nearly 5 kg/m^2 per 10,000 h of operation [2]. Despite advancements in sophisticated erosion coatings and materials, cavitation erosion remains a major concern for scientists and engineers, particularly in the marine industry [3–13]. Cavitation erosion, involving microstructural deformation and localized stress due to cavitation collapse, adversely affects critical components like propeller blades and impellers, resulting in performance decline [14]. Pressure fluctuations during propeller blade rotation create gas/vapour cavities that violently collapse, generating shock waves and high-speed liquid jets, causing hydrodynamic impact pressures exceeding 1 GPa and forming incubation pits [15–24]. Factors that determine the choice of material for propellers include physical and chemical properties, resistance to corrosion, lightweight design feasibility, manufacturing technology, operating efficiency, production cost, and working environment. In terms of mechanical properties, high tensile strength, hardness, toughness, ductility, and fatigue strength are the most desirable. Standard propeller/impeller materials comprise low-carbon, low-alloy or duplex stainless steel, manganese bronze, nickel aluminium bronze (NAB) and newly identified aluminium alloys, composites and advanced polymeric materials [12,25–29].

Aluminium casting alloys have frequently been used as an alternative material for manufacturing valves, piston heads, cylinder blocks, water/fuel pumps and propeller blades etc., owing to the benefits of their low density, high specific strength, corrosion resistance, good casting properties and design flexibility [30]. Table A in the Appendix shows a comprehensive list of casting Al alloys (unless otherwise mentioned) and other Al based materials in addition to the standard marine propeller material, i.e. NAB, used for studying cavitation erosion response in distilled water utilising ASTM G32 standard. The list shows the erosion rate measured in terms of typical mass loss rate (mg/h) and/or mean penetration depth (μm/h) obtained after 1 h of ultrasound exposure for materials processed and prepared using an advanced processing route including but not limited to ultrasonic melt treatment (UST), ultrasonic

* Corresponding author.
E-mail address: apriyadarshi@brookes.ac.uk (A. Priyadarshi).

https://doi.org/10.1016/j.triboint.2023.108994
Received 27 June 2023; Received in revised form 26 September 2023; Accepted 28 September 2023
Available online 29 September 2023

shot peening (USP), annealed/recrystallized and/or tempered, anodised, laser shock processing with (LSPwC) and without (LSP) ablative coating, micro arc oxidation (MAO), mechanically alloyed (MA), additively manufactured (AM), forged and hot isostatic pressed (HIP). While NAB alloy outperforms the others as the most erosion resistant material, some of casting and wrought Al alloys perform just as well or even better at times, as compared to any alloy post-processed through laser/coating and/or heat treatment (see Table A). Compared to wrought (heat--treated) alloys that need to be machined from larger ingots/billets with significant material waste, as-cast Al alloys provide additional advantage in terms of net-shape forming through castings, cost-effectiveness, reduced risk of surface distortions/wrapping encountered during hear treatment, better leak resistance and shorter manufacturing lead time; thus offering a sustainable and efficient way of developing marine equipment parts with complex shapes such as propeller/impeller blades.

Pure Al, often used as a model material, has been investigated for cavitation-induced damage mechanisms [31–34]. The cavitation erosion mechanism of hard Al-Zr tri-aluminide primary intermetallics has been explored, elucidating the formation of micron-sized cracks, protrusions, and plastic pits as a result of repetitive cavitation bubble implosions on their surface [35]. Studies on various Al alloys, such as Al-Si, Al-Cu, Al-Mg, and Al-Zn-Mg-Cu, showed microstructure's impact on erosion mechanisms [36–41], indicating alloying effects on erosion behaviour from uniform surface erosion to the formation of pits with fatigue-like striations and micron-sized pits [36]. Cavitation erosion severity is influenced by both material properties and the working environment. Corrosive media like saltwater can increase mass loss in pure Al by about 20% after an hour of cavitation exposure [41,42]. Similarly, the eroded mass loss of as-cast NAB alloy rose by approximately 6% when exposed to corrosive seawater [43]. Whether it is sea or fresh water, the propellers/impellers and hydraulic pumps often operate within a large range of temperatures (0–70 °C), reflecting, for example, moving from the northern to southern hemisphere. Climate change has also affected to a great extent the temperature and physical properties of water bodies on Earth [17]. Although the liquid temperature can have obvious implications on the material property and corrosive effects and subsequently erosive effects, cavitation dynamic intensity can also be greatly affected. It is known that the water vapour pressure dramatically increases with temperature, thus amplifying the chances of more cavitation events. Studies have shown varying erosion rates at different temperatures, with the peak erosion occurring around 30–60 °C [44–51], emphasizing the intricate role of temperature in cavitation effects.

Despite such extensive work on understanding the cavitation erosion of different Al alloys under specific working environments, the effect of liquid temperature on the erosion response of as-cast alloys has been only vaguely understood and seldom related to the quantified cavitation behaviour, thus still remaining a subject for further exploration. Thus, the present work aims to fill this research gap by assessing the ultrasound-induced cavitation erosion behaviour of different as-cast (A356.2, A380) aluminium alloys in a range of water temperatures (10–50 °C) quantified in terms of the induced acoustic pressures and the resulting erosion rate. We additionally draw a distinct comparison of the surface degradation and erosion resistance between as-cast alloys with a work-hardened wrought AA6082 alloy under aggressive cavitation condition despite its less-than-ideal suitability for marine components due to factors such as manufacturing cost and materials sustainability.

2. Experimental methodology

2.1. Materials preparation

The materials investigated in this research include three as-cast Al alloy samples, i.e., A356.2, A380, which were produced using gravity die casting process, and one extruded sample of an AA6082 T4 (naturally aged) alloy supplied by Constellium. Chemical composition, density and Vickers hardness of the studied materials are presented in Table 1. Density measurements were done using Archimedes principle while Vickers hardness test of the specimens was conducted according to ASTM E384 standard using the microhardness tester (Buehler Micromet) by applying 10 N load for 15 s. The measurements were taken from 5 different locations on the specimens and the results were averaged as shown in Table 1.

Specimens of size L: 25 × W: 25 × T: 6 mm with a tolerance of ± 0.2 mm were cut using a SiC rotating disc. To maintain comparable conditions and minimum surface damage, surfaces of specimens were ground (using P240, P400, P800, P2400 SiC abrasive paper) and polished (using 9 and 3 μm diamond abrasive and 0.06 μm silco colloidal paste) to a maximum initial surface roughness (S_a) of 0.7 ± 0.1 μm using an ATM Saphir 520 polishing machine. The polished specimens were subsequently anodized with Barker's solution (5% HBF_4 water solution) for about a minute at 20 VDC to reveal the grain structure of the microstructure under polarised light using VHX700 digital microscope (Keyence Ltd.).

2.2. Experimental setup

Ultrasonic cavitation erosion experiments based on an indirect vibratory cavitation test were performed according to ASTM G32 standard [52]. An ultrasonic transducer operating at a frequency of 20 kHz and at 88% of its maximum input power was used to achieve a 50-μm peak-to-peak amplitude. The ultrasonic cavitation was generated in the test liquid through a titanium cylindrical sonotrode of 22-mm in diameter. Studied samples were fitted onto the bottom of a glass container having dimensions of approx. L: 75 × W: 75 × H: 175 mm filled with de-ionised water. It is important to note here that even though pure water erosion experiments might not replicate specific industrial applications, for example, in marine related scenarios, they provide a vital foundation for developing a comprehensive understanding of erosion mechanisms that can be further extended to address the complexities of real-world scenarios like in seawater. The vibratory horn was immersed about 20 mm below the liquid surface. The distance between the horn tip and the surface of the specimen was maintained at around 0.5 mm as per the ASTM G32 standard, using an adjustable lift arm and a gauge filler gap measuring blade to account for any structural tilt of horn and sample surface. The experiment was periodically interrupted at fixed intervals to determine any temporal volumetric (mass) changes. The cumulative cavitation exposure time for each sample was 60 min. The periodicity of interruptions used during the cavitation test is shown in Table 2. These intervals were deliberately chosen to have more number of data points during the inception/incubation stage to better resolve pitting/cavitation development than during large exposure period.

The primary means of erosion damage assessment was the cumulative mass loss measured periodically by weighing the specimen. The observed mass loss was further utilised to evaluate the erosion resistance in terms of nominal incubation period, mass loss rate and instantaneous mean depth erosion rate (MDER) defined as the ratio of mass loss to the product of density, eroded area and exposure time. After each cavitation exposure period, the specimens were cleaned using isopropanol, air-dried and weighed. Measurement of mass loss (mg) at a certain time interval involved taking 7 readings on an Adam Highland HCB 123 Precision Balance scale with an accuracy of 0.1 mg. Subsequently, the minimum and maximum values were discarded and the arithmetic average was calculated from the remaining 5 readings. The extreme values were disregarded to ensure robustness in our data analysis and to mitigate the influence of potential anomalies and provide a representative measure of the mass loss/erosion rates.

The erosion experiments were performed between 10 and 50 °C at intervals of 10 °C. The temperature of water was maintained within ± 1–2 °C throughout the experiment using a re-circulating cooler (Cole Parmer Stuart SRC5) connected to the outer container (L: 32 × W: 21 × H: 21 cm) filled with water and anti-freeze coolant mix (1:1 ratio)

Table 1
Chemical composition, density and hardness of the Al alloys used in this study.

Material	Composition (%)												Density (g/cm^3)	Hardness (HV_{10})
	Si	Fe	Mg	Mn	Cr	Cu	Ni	Sn	Zn	Zr	Ti	Al		
A356.2	6.5–7.5	0.15	0.4	0.1	-	0.03	0.05	-	0.07	-	0.1	Bal.	2.67	52 ± 5
A380	7.5–9.5	1.3	0.1	0.5	-	3.5	0.5	0.35	3	-	-	Bal.	2.71	94 ± 5
AA6082	0.7–1.3	0.0–0.5	0.6–1.2	0.4–1.0	0.0–0.25	0.1–1.1	-	-	0.0–0.2	0.05–0.15	0.1	Bal.	2.7	96 ± 2

Table 2
Periodicity of cavitation exposure used for erosion experiments of Al alloys.

Exposure time (min)	0 – 6	6–14	14 – 20	20–40	40 – 60
Interval (min)	1	2	3	5	10
Data points	6	4	2	4	2

through hosepipes. The temperature was monitored and recorded using a PRO RS53 digital thermometer attached to a thermocouple. To check for any temperature fluctuations due to potential hydraulic friction, a thermocouple was specifically positioned close to the sample and the sonotrode tip. After establishing the thermal conditions at which the highest material erosion occurred, a set of specimens from each cast alloys were examined and compared with a wrought alloy using a digital microscope acquiring 3D scans to obtain surface topography and average (S_a) roughness profiles of the eroded area. Electron microscopy was also used to evaluate the surface degradation of samples after 60 min of cavitation exposure using a JEOL JSM-6010PLUS/LA scanning electron microscope (SEM). Prior to SEM imaging, each sample underwent cleaning in an ultrasonic bath of acetone solution. Fig. 1a shows

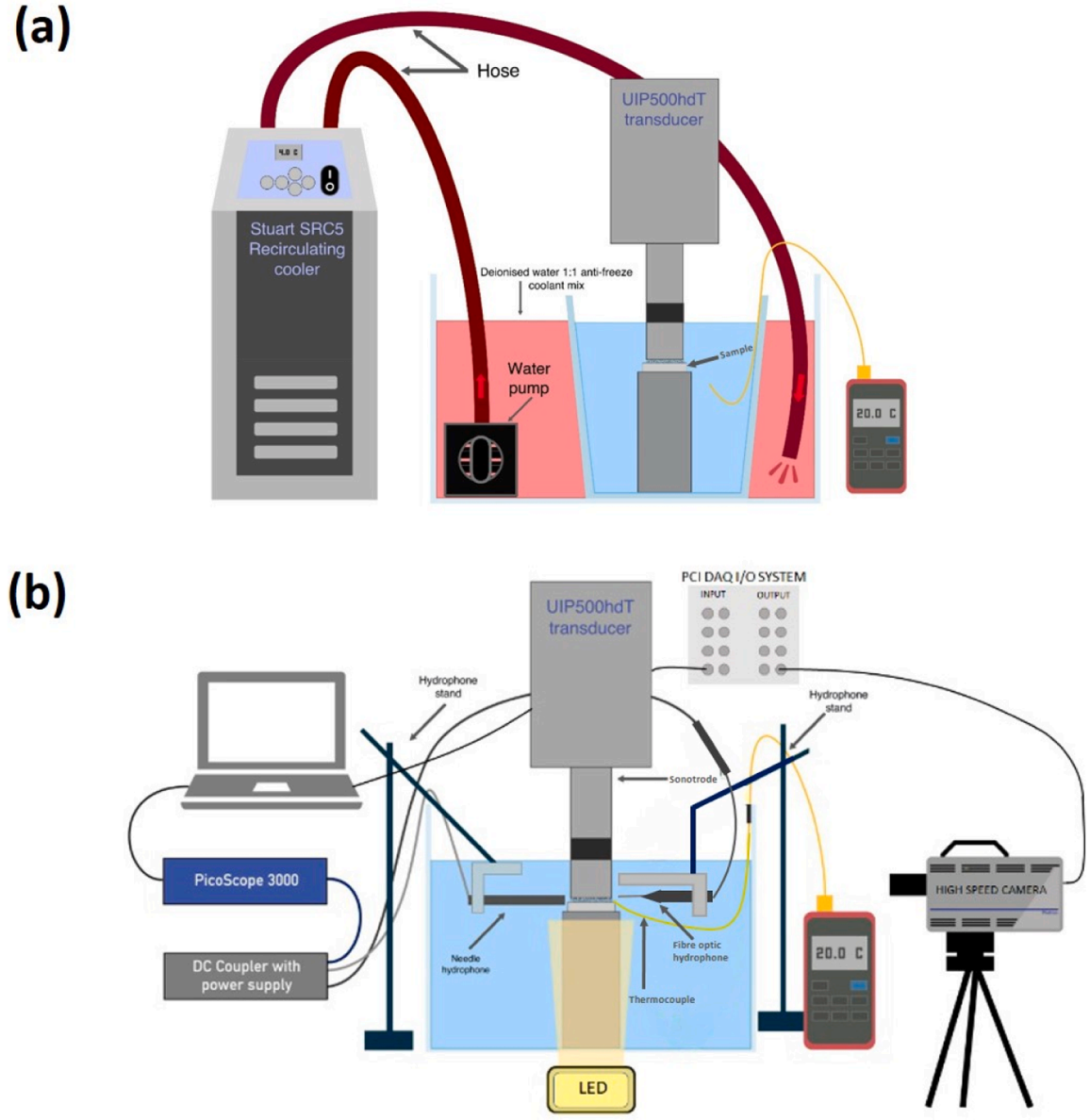

Fig. 1. Schematic of the experimental test rig used for (a) cavitation erosion of specimens; (b) acoustic pressure measurements.

the schematic of the ultrasonic cavitation erosion test rig used in this study.

2.3. Acoustic pressure measurements

An in-situ needle hydrophone (NH) and fibre optic hydrophone (FOH) system synchronised with a high-speed camera were used to detect and observe the acoustic emissions simultaneously. Illumination was provided using high power GS Vitec MultiLED lamp to accurately capture cavitation events and ensure the reliability and comparability of the results. A data acquisition device (DAQ) with a potential of capturing 20×10^6 samples per second was utilised to couple the NH and FOH systems with the high-speed camera through the input/output slot. Both cavitation sensors, i.e. NH and FOH, were placed at the side edges between the sonotrode and specimen surfaces and approximately 5 mm away from the centre of the horn tip. The NH and FOH were calibrated in the low (8 – 400 kHz) and high (0.3 – 30 MHz) frequency, respectively, to account for the emissions received from both cavitation bubbles and shock waves. The sensitivity of both the sensors can be found elsewhere [35]. The emissions were captured from 60 waveforms each of 2 ms duration. The synchronised measurements were recorded from the beginning of the cavitation activity until the emissions were stabilised.

The post-processing of the raw (voltage-time) signal acquired from the sensors was carried out by Fast Fourier Transformation (FFT) using an in-house developed MATLAB code as reported elsewhere [53,54]. The desired acoustic pressure magnitude across the time domain was obtained after subtracting the background noise, and the measurements were linked to the induced cavitation bubble activity from the ultrasonic horn. Fig. 1b shows the setup used for recording the acoustic emissions and synchronised capturing of the bubble dynamics.

3. Results and discussion

3.1. Metallographic analysis

Fig. 2(a-c) shows the optical micrographs of as-cast A356.2 sample exhibiting shrinkage porosity (see Fig. 2b) and a typical structure showing large equiaxed grains (> 1 cm), and phases of eutectic origin: Si, α(AlSiMnFe), π(AlFeMgSi) and Mg_2Si with a total mass fraction of 6.7 wt% (estimated using Thermocalc software with the TCAL4 database). Scheil solidification modelling was utilized to predict the phases present in the as-cast microstructures resulting from non-equilibrium solidification. Fig. 2(d-f) shows the as-cast structure of the A380 alloy showing insignificant amount of porosity evenly distributed between equiaxed grains (up to 1 mm in size), and the phases of eutectic origin: Si, Al_2Cu, Al_7Cu_4Ni, α(AlSiMnFe), and β(AlFeSi) with a total mass fraction of 19.1 wt%. Among two as-cast alloys, A380 also exhibited highest hardness, which maybe because the excess phases are more evenly distributed across the surface with less pronounced Al dendrites (compared to A356.2). This suggests that the distribution of stress applied to the surface could be more uniform in the A380 alloy, potentially leading to enhanced hardness. The extruded AA6082 alloy (Fig. 2(g-i)) shows typical fibre-type elongated grains, little recrystallization and some excess phases at the grain boundaries. The AA6082 alloy predominantly consists of an aluminium solid solution of Mg and Si. The properties of this alloy are significantly influenced by a combination of factors, including the presence of Mg and Si, as well as the effects of deformation processes such as work hardening. While certain surplus phases might emerge due to impurities within permissible limits, their impact on the material properties remains relatively minimal. The phases are likely to be α(AlSiMnFe), π(AlMgFeSi), and β(AlFeSi) that

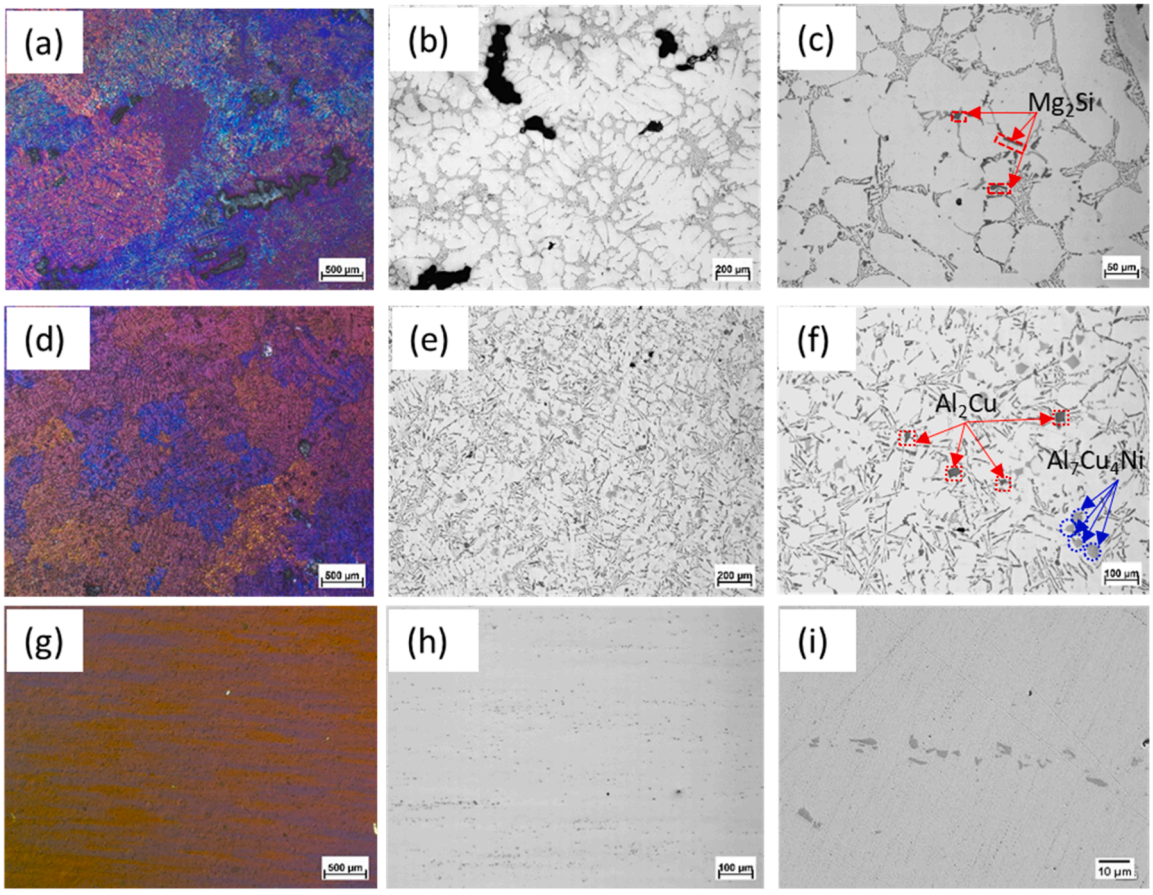

Fig. 2. Optical micrographs showing typical microstructures of as-cast A356.2 (a-c), A380 (d-f) and extruded AA6082 (g-i) prior to erosion testing. Note microsctrures in (a), (d) and (g) are polarised images of anodised specimens.

may have been fragmented and spheroidised because of homogenisation, pre-extrusion heating and extrusion deformation. Since this specimen is not recrystallized, it retains high hardness resulting from work hardening during extrusion followed by natural ageing.

3.2. Ultrasonic cavitation erosion experiments

The erosion response of the as-cast alloys was first measured in a range of water temperatures as mentioned in Section 2.2 and later compared with an extruded AA6082 alloy tested at the temperature of maximum erosion/mass loss. Owing to the erratic nature of the loading encountered during cavitation attack, it is difficult to establish a strong correlation between the material properties and its corresponding resistance to degradation. Therefore, cavitation erosion resistance is often regarded as an independent property of its own and can be assessed based on the cumulative mass loss, incubation period and mass loss/erosion rate [55]. Fig. 3(a-e) shows the cumulative mass loss of specimens subjected to ultrasonic cavitation at different test temperatures. As expected, the mass loss increased with increasing cavitation exposure with incubation period varying in the range of 5 – 20 min depending on the liquid temperature, mechanical properties and alloy composition, after which the erosion increased at a rapid rate. The incubation time was determined based on the onset of significant damage (mass loss greater than 0.5 mg) when exposed to ultrasonic cavitation and has been mentioned in the mass loss-time plots for each alloy. Fig. 3 (a-e) revealed interesting trends in the incubation time at different temperatures specifically for A356.2. At lower temperatures of 10 and 20 °C, the incubation time were relatively longer, ranging from approximately 10 to 12 min (see inset in Fig. 3a and b). However, at intermediate temperatures of 30 and 40 °C, the incubation time decreased to approximately 6 – 8 min, indicating a faster onset of significant erosion. Subsequently, the incubation was found to increase again to approximately 10 min at higher temperatures close to 50 °C. These findings suggest that the A356.2 alloy possessed somewhat better resistance to cavitation erosion at lower temperatures in comparison to intermediate and higher temperature ranges. For A380, however, the incubation time remained in the range of 15 – 20 min and did not exhibit any significant change with temperature. Cavitation erosion resistance can also be effectively characterized by analysing the mass loss rate observed after the initial stages of erosion and during the acceleration period. In the case of A356.2 alloy (Fig. 2f), once the incubation period elapses, the mass loss rate reaches its peak at 30 °C and sustains this high rate for an extended duration, peaking at approximately 12 mg/h. It is important to highlight that even during the incubation period, the mass loss rate remains detectable but not pronounced, suggesting the presence of cavitation activity that has yet to cause substantial damage. Comparatively, A380 alloy (Fig. 2g) exhibits slightly different behaviour. While the incubation period variation remains relatively consistent across temperatures, a notable mass loss rate of up to 4 mg/h is observed within the intermediate temperature range of 30–40 °C. This finding underscores that elevating the temperature levels significantly accelerates cavitation erosion for both the alloys. However, a critical threshold emerges, notably around 30 °C, at which the transition from the incubation phase to significant erosion occurs more rapidly. This critical temperature boundary markedly diminishes the cavitation erosion resistance of the alloys.

At all temperatures, the A380 alloy exhibited the higher erosion resistance (highest incubation period and lowest mass loss rate) than the A356.2 alloy. Amongst the tested temperatures, the total eroded mass was found to be maximum at 30 °C irrespective of the material (closely followed by the exposure at 40 °C) with A380 showing the lowest cumulative mass loss. The relation between the mass loss and the temperature was found to be non-linear and exhibited mixed variation. Fig. 3f shows the calculated MDER of different alloys at specific water temperatures in the units of μm/h. It can be seen that the erosion rate dropped by almost 20% from 10 °C to 20 °C for A356.2 alloy, while it decreased by ~28% for A380 alloy. To some extent, the erosion rate reached maximum between 30 and 40 °C for both alloys as observed from the mass loss data. The erosion rate for all alloys further decreased at 50 °C. Results are in close agreement with results reported elsewhere [44,47]. It is worth noting here that temperature corresponding maximum material damage can vary depending on the material being investigated, liquid environment and the involved measurement test rig with different operating parameters such as exposure time, stand-off distance etc. For example, Plesset [44] previously observed that maximum material erosion in case of mild steel occurred between 30 and 40 °C and for 24S-T4 alloy, between 40 and 50 °C. Note that the erosion measurement in this study was made after only 15 min of cavitation exposure. Hattori et al. [47], on the other hand, found that the MDER for pure Al and Cu is maximum between 40 and 50 °C. In our study, we also employed a unique in situ real-time acoustic pressure monitoring system that allowed us to accurately capture the pressure

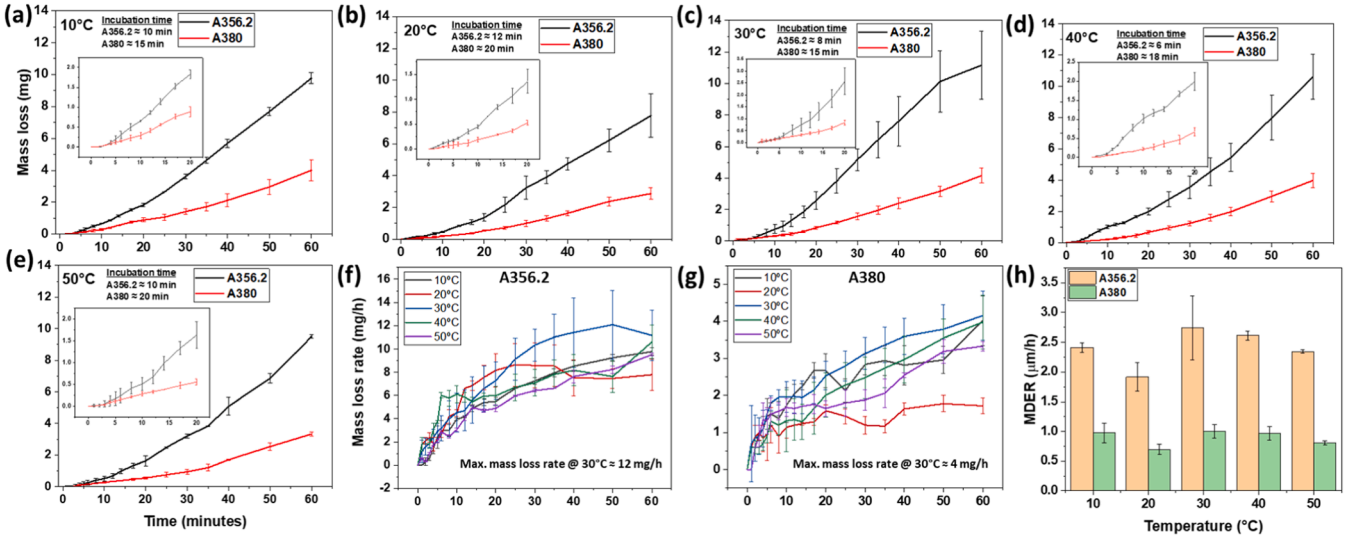

Fig. 3. Cumulative mass loss (a-e) and mass loss rate (f-g) as a function of exposure time measured for the examined alloys subjected to ultrasonic cavitation erosion tests measured under water bulk temperatures ranging from 10 °C to 50 °C and (h) effect of temperature on the mean depth erosion rates obtained after 1 h of treatment.

emissions (see Fig. 4 below) and provide not only qualitative (as mostly observed in erosion related studies) but also quantitative evaluation of the temperature response on the erosion damage by cavitation impact in due time. This new method of assessing cavitation dynamics allows for more accurate and quantitative measurements and could be used to further study the effect of temperature on cavitation erosion, and to better understand the mechanisms of erosion damage.

The extent of material erosion is dictated by the severity of cavitation process, which is based on the bubble dynamics and the resulting pressure field from the cavitation collapses. Fig. 4a shows the plot of acoustic pressure induced from ultrasonic cavitation at different temperatures captured by both in-situ needle hydrophone (NH) and fibre optic hydrophone (FOH) at intervals of 2 °C and 10 °C, respectively. Measurements from the low frequency sensor, i.e. NH, represent the dynamic root mean square (RMS) pressure from the incident wave, harmonics and cavitating bubble emissions (including any sub- and ultra-harmonics), whereas measurements from the high frequency sensor, i.e. FOH, correspond to the maximum shock wave pressure amplitude generated from bubble implosions. It is evident from Fig. 4a that the generated pressures from both the cavitating bubbles and emitted shock waves within the cavitation zone (region between the horn and the specimen) were maximum (~ 2000 and 350 kPa, respectively) at 10 °C and then dropped to minimum (~ 950 and 105 kPa, respectively) close to 20 °C. Note the difference in the pressure amplitudes arising from the bubbles and shock waves with decrements of ~74% and ~52%, respectively from 10 °C to 20 °C. The reasoning for this large drop is related to a drop in pressure magnitude due to acoustic shielding effect as described in [51]. The phenomenon of acoustic or cavitation shielding arises as a consequence of a complex interplay of factors that influence the behaviour of cavitation bubbles, ultimately impacting the acoustic pressure field in the surrounding medium. This shielding effect is a result of a process wherein bubbles in the upstream region, closer to the cavitation source, shield/cushion those present in the downstream region. Here, the bubbly cloud attached to the ultrasonic horn restricts the propagation of shock wave emitted from their collapse to the outside regions. Thus the bubbles present in downstream region do not get affected by the propagating shock fronts and, therefore, do not implode. This interaction leads to the attenuation of the acoustic pressure field weakening its intensity. Acoustic shielding is intricately linked to the number of cavitation bubbles present in the medium and their relative location. The greater the number of these bubbles, the higher the degree of absorption and scattering of incoming sound waves, resulting in a substantial reduction in the acoustic field intensity. The concept of acoustic shielding is widely acknowledged and has been extensively studied elsewhere [56,57]. The decline in acoustic pressure as temperature increases is likely attributable to an upsurge in both bubble quantity and vapour pressure contained within the bubbles. This phenomenon consequently reduces the likelihood of their collapse. Furthermore, elevated water temperatures promote the generation of bubbles from dissolved gas (air) nuclei, causing the pressure within these bubbles to exceed the vapour pressure corresponding to the given temperature. As a result, the chances of sudden cavitation collapse decrease. Tzanakis et al. [58] experimentally demonstrated the significance of vapour pressure on cavitation development and found that a liquid with higher vapour pressure would exhibit lower cavitation noise intensity than the one with lower pressure. Additionally, higher solution temperatures lead to a reduction in the surface tension of bubbles, further contributing to a decrease in the occurrence of bubble implosions [59]. At lower temperatures, however, the reduced thermal energy within the system restricts the formation and growth of cavitation bubbles, leading to a decrease in their quantity. While a lower bubble count might suggest reduced cavitation activity, the intriguing aspect lies in the significantly intensified implosion of these fewer bubbles at lower temperatures, as extensively documented in multiple studies [60–63]. As the liquid temperature increases, the diffusion rate of dissolved gas accelerates, significantly affecting the rate of bubble nucleation [64,65]. This change in the nucleation rate is likely attributed to the reduction in the liquid surface tension due to increased gas solubility at elevated temperatures. Another explanation is that the decrease in surface tension diminishes the tensile strength required for bubble growth [66]. Conversely, the reduction in surface tension further reduces the intensity of cavitation due to the decreased stability of bubble shape. Consequently, enhanced gas molecule transport within a bubble, driven by either a higher partial pressure of vapour or gas, results in the dampening of cavity pulsation and promoting cushioning of collapses as described previously. It has also been reported that vapour collapses typically have shorter lifecycles, lasting only one or two acoustic cycles, before culminating in intense implosions that generate higher pressure emissions [67]. Thus, to achieve optimal cavitation bubble implosion, it is essential for the liquid to contain minimal dissolved gas. Unless the liquid is thoroughly degassed, nearly all liquids below their boiling point naturally contain dissolved gas. During the growth phase of cavitation bubbles, gas from the liquid can infiltrate these bubbles via a process referred to as "rectified diffusion" [68]. This inflow of gas within the cavitation bubble acts as a counterbalance, inhibiting violent implosion at elevated temperatures. Thus, the severity of the implosion of these gas (air) filled bubbles during their collapse phase would lessen and rather a cushioning (shielding) effect would be produced, causing the pressure

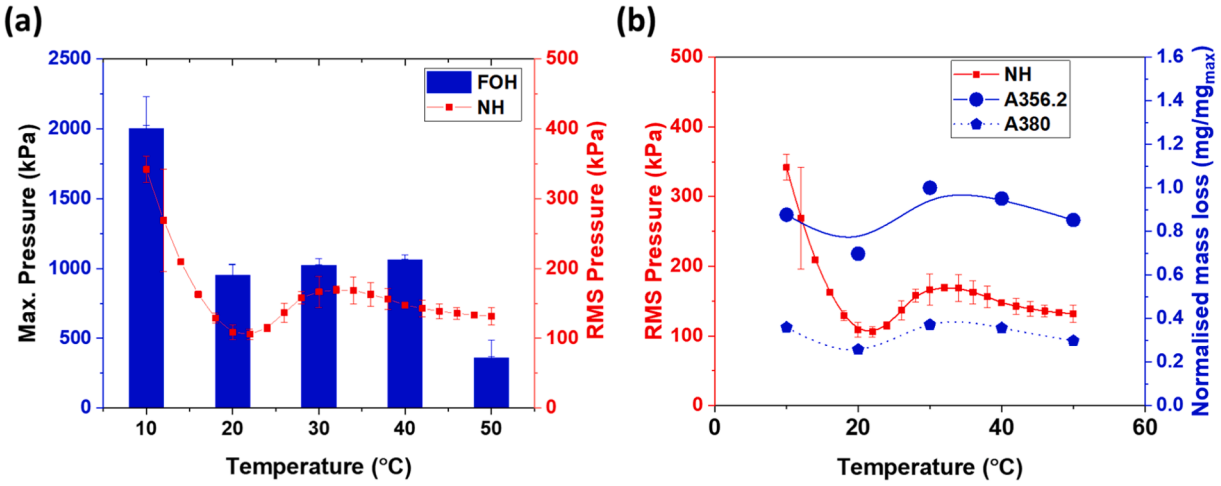

Fig. 4. Effect of temperature on (a) the acoustic pressure field generated within the cavitation zone recorded using FOH and NH; (b) RMS pressure and normalised mass loss for the examined alloys after 1 h of exposure.

magnitude to drop significantly. This is especially apparent in the shock pressure recordings where the pressure drop at 50 °C is significant with values less than 500 kPa (see Fig. 4a). However, at intermediate temperature of 30 °C, the induced pressure field is close to 1 MPa, which signifies the trade-off between the emergence of vapour and gas bubbles with increasing temperature, which in turn governs the pressure dynamics within the liquid medium. The cavitation induced pressure as measured by the NH then increased around 30–40 °C up to a value of 160 kPa, while the shock pressure only slightly increases followed by decrease at 50 °C. These pressure trends are in good agreement with the recent work of Morton et al. [51], where the acoustic pressure measured with a calibrated cavitometer device was observed to be largest at 10 °C, followed by drop at 20 °C and subsequent increase around 30 °C, using a similar 20 kHz transducer with an operating peak-to-peak amplitude of 57 μm.

Usually, it is expected that the higher the generated acoustic pressure, the more will be the material erosion. However, this was not the case in our experiments as seen from Fig. 4b especially at 10 °C. Fig. 4b shows the plot of variation in recoded RMS pressure and the measured eroded mass loss (normalised to that of maximum value) of different test specimens with respect to temperature. It can be observed from the figure that erosion is highest for temperatures in the range of 30 – 40 °C, even when the cavitation induced pressure is not maximum. The phenomenological reason for this interesting observation is inherently linked to the cavitation bubble implosion characteristics that in conjunction with emitted liquid microjets and shock wave dynamics play a dominant role in inducing surface erosion of materials. A detailed explanation has been provided in the next paragraph. These observations [51,69] are also in good agreement with results reported elsewhere [44,45]. The erosion damage induced by cavitation is primarily attributed to the repeated impact of shock pressure pulses and water hammer pressures generated by the liquid microjet impact upon bubble collapse on the surface of the component [10,46,70–72].

Interestingly, the mass loss trend follows that of the RMS pressure. At 10 °C, where the registered pressure is maximum, the erosion is high but not maximum as the cavitation zone development and amount of cavitation cloud are restricted just under the sonotrode as previously reported in [69] and even if shock wave propagate undisrupted in the liquid medium, the implosion events are confined only to a narrow region and in lesser number, thus the damage is not significant/maximum. At 20 °C, where the overall pressure dropped, erosion rate was also affected accordingly and mass loss was equivalent/proportional to that of pressure drop. At 30 °C, as the pressure further increased, the overall mass loss increased, reaching a maximum for all cases followed by similar values at 40 °C. Finally at 50 °C, a significant drop in maximum pressure was observed followed by the drop in mass loss as well. Kaur et al. [69] recently reported that at low liquid temperatures, i.e. ~10 °C, the formed bubbly clouds beneath the sonotrode tip were less prominent and comparatively smaller, thereby allowing the shock fronts to propagate within the cavitation zone undisturbed raising the shock pressure amplitude but inducing lesser damage as being lower in numbers, i.e. smaller cavitation zone. Conversely, at higher temperatures, i.e. ~50 °C, the bubble clouds formed were much larger, covering the entire substrate that promoted cushioning of the propagating shock fronts and microjets as a result of non-collapsing (partial) deflations [73] thus alleviating the aggressiveness of the cavitation impact resulting in lesser/suppressed mass loss (Fig. 3b).

This partial deflation is caused by the interaction between the bubbles/bubble cloud behaviour and the surrounding liquid environment. Instead of fully collapsing during the compressive phase of the vibration, the bubble's collapse is hindered due to factors such as the inertia of the surrounding liquid. Non-collapsing deflations alter the dynamics of cavitation bubble collapse and generated acoustic emissions. This alteration mitigates the aggressiveness of the cavitation impact on the material surface resulting in suppressed mass loss. Thus cushioning effect generated during non-collapsing deflations helps explain why, even though these bubbles do not fully collapse, they still play a role in the overall erosion process, albeit with reduced intensity. Thus, the critical temperatures must exist somewhere between the two extremes, where the formed bubble cloud is large enough to allow sufficient amount of shock and liquid jet impacts and, therefore, the erosion progresses much faster within this temperature range. Therefore, based on this study, the temperature regime favourable to cavitation damage is close to 30 °C, where the erosion is maximum for all the cases. It has been reported that the cavitation intensity and the induced damage at different temperatures is dictated by the cushioning effect from the internal gases (dissolved air) [44]. In another study, it was found that the cushion from the gases would be minimised at an intermediate temperature of around 34.5 °C, which is associated with maximum material removal [45]. Therefore, it is also reasonable to argue that the erosion mechanism is somewhat a trade-off between the amount of shocks reaching the sample surface and the collapsing events across the surface promoting shielding effect [56], which is sensitive to different temperature regimes. The fundamental governing mechanism of cavitation inception and erosion has been explained in some detail elsewhere [35,74]. It has been reported that as the cavitation initiates, the pre-existing bubbles under ultrasonic excitation tend to chaotically oscillate and undergo continuous splitting and coalescing near the solid boundary releasing shock waves and multiple microjets producing water-hammering effect [70].

In-situ high-speed optical imaging and acoustic emission characterisation could not reveal any noticeable difference in the cavitation field dynamics for different bulk liquid temperatures perhaps due to the small separation distance between the horn and the alloy specimen. Fig. 5 (see supplementary video) shows the sequences of synchronised high-speed images (Fig. 5(a-f)) and the acoustic pressure (Fig. 5g) measured using NH captured at 30 °C. The first frame at time t = 0 shows the sonotrode tip and the alloy specimen with an NH located between the gap (see Fig. 5a). The frame also shows multiple air/gas bubbles that may have heterogeneously formed over the substrate (sample) surface. Note, the observed cavitation activity and the resulting pressure measurements remained independent of the studied specimen because of the short recording duration. With the introduction of ultrasound, these gas bubbles underwent vigorous oscillations and coalesced with neighbouring pulsating bubbles as shown in Fig. 5b. It can also be seen that very first cavitation collapses occurred close to 30 ms with very few bubbles formed across the sample surface (indicated with red arrows). Simultaneously, the pressure peaks also started to appear in the pressure-time profile resulting from the acoustic emissions (see supplementary video) and shock wave surges [67]. Subsequently, more bubbles were nucleated and the formed microbubble clusters grew in size while undergoing splitting and coalescing (indicated by red arrows) with increased ultrasound exposure until t = 63.88 ms covering the region below the sonotrode tip (Fig. 5(c-e)), similar to the observations previously reported in [74]. The populated bubble cloud is formed with regular collapses that contribute to the increase in pressure field up to a point of about 300 kPa. The generated cavitation and associated pressure peaks subsequently became stabilised beyond t ≈ 64 ms (Fig. 5f). The stabilised pressure field is marked by the appearance of periodic shock wave peaks from the subharmonic (major peaks) and ultra-harmonic (minor peaks) collapses and non-collapsing deflations as recently explained in [57]. It is important to note here that between 30 and 75 ms, which is equivalent to almost 900 acoustic cycles (50 μs per cycle), multiple collapsing events occurred at similar locations across the sample surface (see large bubble clusters in Fig. 5(c-f)). Therefore, it is possible that those specific locations experienced severe cumulative cavitation impact, thus causing plastic deformation and erosion of the formed plastic pits as previously seen in [15,18,23]. While primary damage happens due to cavitation cloud collapse as shown by Wang et al. [75], small bubbles (visible as black dots in Fig. 5) collapsing both before and after the primary cloud also significantly contribute to the erosive energy of cavitating liquid. Though not individually as forceful as larger bubbles, their numerous presence and large spatial distribution

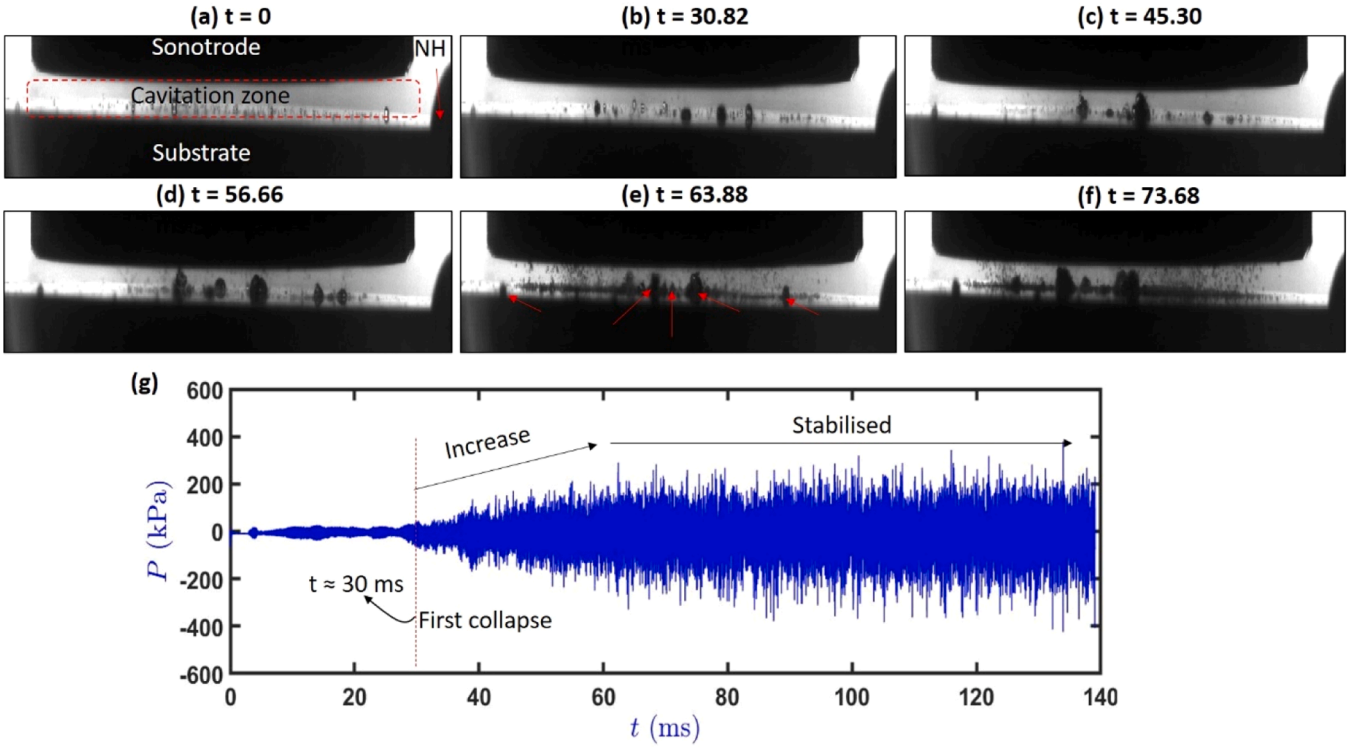

Fig. 5. Sequence of high-speed images (a-f) of the cavitation activity occurring between the horn and the specimen separated at 30 °C. The synchronised acoustic pressure (g) is obtained from the generated cavitation emissions measured using NH.

across the material surface can collectively enhance the erosion effect. The cumulative impact of these small bubbles hitting the surface can further lead to gradual damage, causing surface deterioration over time. Their size also enables them to reach confined spaces and crevices that larger bubbles might miss, initiating micro-cracks and material removal. While large bubbles create visible shock waves, the simultaneous collapse of small bubbles also generates intensified shock waves and liquid jets [76]. These waves, interacting with the material, induce cavitation-induced fatigue and erosion, particularly in areas with existing pits or damage. This is the reason as to why in some areas across the sample surface, the formed craters are much deeper (as will be seen later in the Section 3.3). Under these circumstances, the cavitation bubbles would also have more proclivity to impact regions with deep craters and pits. Thus the probability of spatial collapse at specific locations is likely to be higher for initiating and spreading the damage across the surface. The localized damage in the form of accumulated pits are generated mainly due to impingement of high-speed liquid jets that in conjunction with shock waves lead to development of craters [15]. These high pressure shock waves from the imploding bubbles and bubble cloud under the horn-tip further loosen the impacted areas with damage propagating in a fatigue-like manner. Ogloblina et al. [77] confirmed through numerical simulations that both primary (bubble cloud) collapse and secondary implosions could potentially contribute to material erosion.

Supplementary material related to this article can be found online at doi:10.1016/j.triboint.2023.108994.

After identifying the temperature response to erosion and noting that bulk temperature close to 30 °C contributes to maximum erosion for as-cast alloy specimens, we now compare their mass loss and surface roughness profile measured in terms of S_a with an extruded AA6082 alloy at this temperature. This alloy represents an alternative way of manufacturing through deformation and machining. Fig. 6(a-c) shows the cumulative mass loss and change in S_a against different exposure time for each tested Al alloy. As expected, after 1 hr of cavitation exposure, the surface roughness of all specimens tends to increase along with the mass loss. Interestingly, for the as-cast A356.2 (Fig. 6a), the mass loss showed a strong correlation with S_a curve with short incubation period interval having correlation coefficient of 0.995, demonstrating its poor erosion resistance as compared to the A380 alloy (Fig. 6b), which seemed to show a relatively longer incubation period of approximately 20 min in terms of S_a value in comparison to the mass loss, with the correlation coefficient of 0.961. It is interesting to note that after 1-hr exposure, the eroded mass for the extruded AA6082 alloy was almost 4 times lower compared to the worst performing alloy, i.e. A356.2. The extruded AA6082 alloy (Fig. 6c) also showed an almost negligible correlation of S_a with mass loss with the longest incubation period of almost 40 min signifying its strong erosion resistance. It can be seen that after 40 min of cavitation exposure, the trend for mass loss and S_a are pretty much similar in all Al alloys meaning an extended cavitation exposure would result in even higher correlation coefficient, almost tending towards unity.

It is worth mentioning here that according to general consensus [78–81], it is understood that the removal of hard (intermetallic) phases from the bulk (soft) matrix during erosion causes the surface roughness to increase and was found to be correlated with erosion rate/exposure time as in the present study (Fig. 6). Recent study by Krella [82], further highlighted that the presence of hard particles within a ductile matrix can have significant implications for cavitation erosion resistance, depending on the size and shape of these particles. Particularly, lamellar (needle) particles can act as stress concentrators and be more detrimental than spherical particles. When cavitation bubbles collapse near the surface, the resulting high pressures and stresses generated from repetitive impact of microjets can induce the preferential removal or cracking of hard intermetallic particles and induce plastic deformation caused by dislocation movement [36,71,83]. As these hard or brittle phases are removed during cavitation erosion, the surface undergoes transformations that manifest as pits, craters, and other forms of surface irregularities. The removal of these phases leads to an uneven material removal rate across the surface, contributing to the development of increased surface roughness. However, there have been investigations

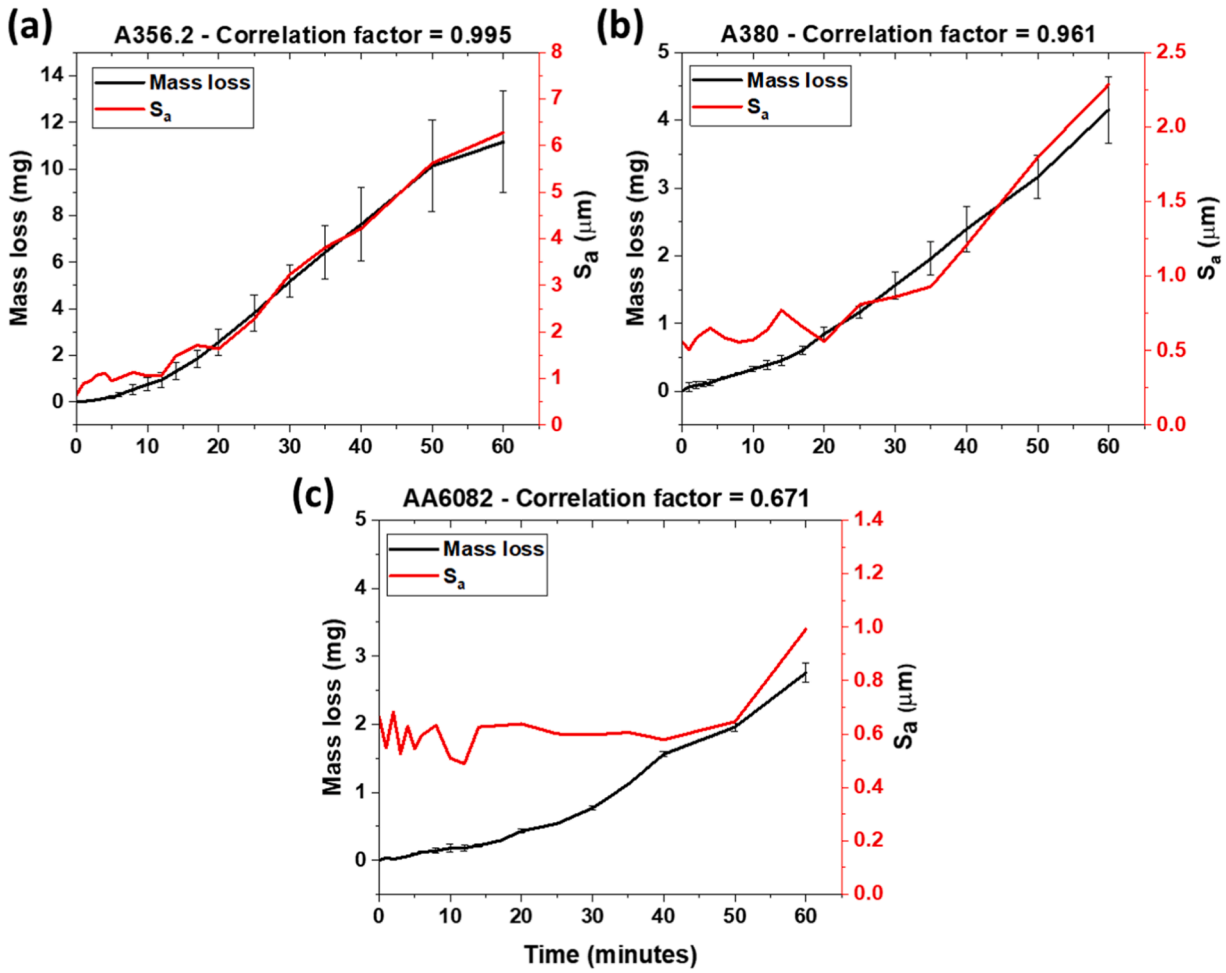

Fig. 6. Results of cavitation exposure at 30 °C on the variation of mass loss and its correlation with surface roughness measurements (S_a) with respect to exposure time for different Al alloys.

that oppose this very notion [84,85]. For example, Chiu et al. [84] revealed that the rate of increase in surface roughness is high during the initial period of exposure and subsequently declines with further increase in erosion time. This kind of behaviour has been linked to changes in the number and geometrical features of the formed cavitation pits as the erosion progresses.

Although a direct correlation between the hardness and mass loss during erosion is still debatable, studies have shown that cavitation-induced erosion is significantly altered by the changes in hardness of the sample [86,87]. Ideally, a higher hardness would essentially result in less surface damage in terms of eroded mass and vice versa. On the other hand, it has been postulated that high pressure pulses produced by the hydrodynamic effects of collapsing cavitation bubbles can induce strain hardening within the localised regions of impact. The build-up of strain in those impact zones can further cause dislocation to form and entangle, further increasing the hardness. In our case, the overall erosion response of the studied Al alloys at 30 °C was observed to linearly correlate with their corresponding initial hardness with $R^2 \sim 0.98$, as shown in Fig. 7 signifying that hardness may act as an indicator for erosion performance prediction in Al alloys.

The impact of hardness on the cavitation-induced degradation of ferrous and non-ferrous materials have been investigated in great detail elsewhere [86,88], where an exponential correlation was found between surface hardness and damage (volume loss). It should be noted that erosion response of materials depends on several factors other than hardness such as the underlying degradation mechanism, micro/crystal structure, strength/toughness, cavitation intensity and apparatus used

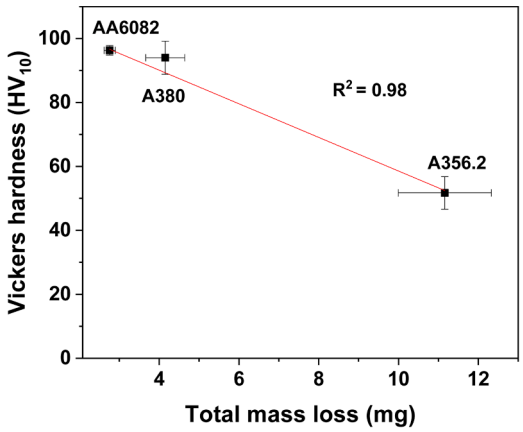

Fig. 7. Correlation between total mass loss measured after 1 h of exposure and initial hardness of studied alloys.

during such investigations. Therefore, to assess the comparative performance of the studied alloys with other materials in the same category, we plotted the specific cavitation erosion resistance of different aluminium alloys, aiming to identify an potential alternative material for the production of complex-shaped hydraulic/marine equipment. Fig. 8 presents a normalized bar chart comparing the erosion performance of various Al alloys [6,21,31,89–95], obtained through a

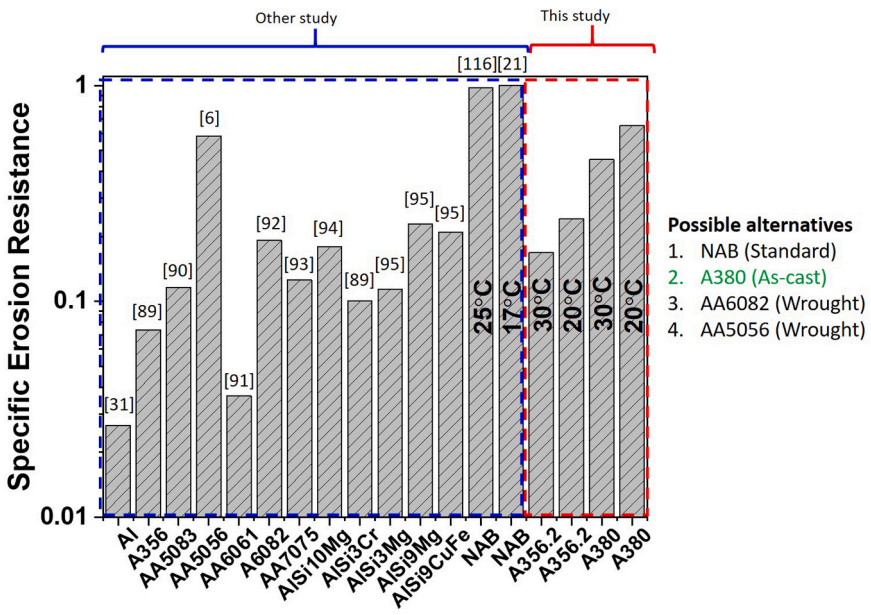

Fig. 8. Comparison of specific erosion resistance of Al alloys with extruded AA6082 and standard NAB obtained after 1 h of exposure.

vibratory test setup similar to that employed in our study. The specific erosion resistance of each alloy was calculated by dividing the mass loss rate by its respective density after one hour of testing. Pure Al exhibited the lowest erosion resistance, while NAB demonstrated the best performance among all the alloys, followed by AA5056 and extruded AA6082. A380 also displayed favourable erosion resistance, likely due

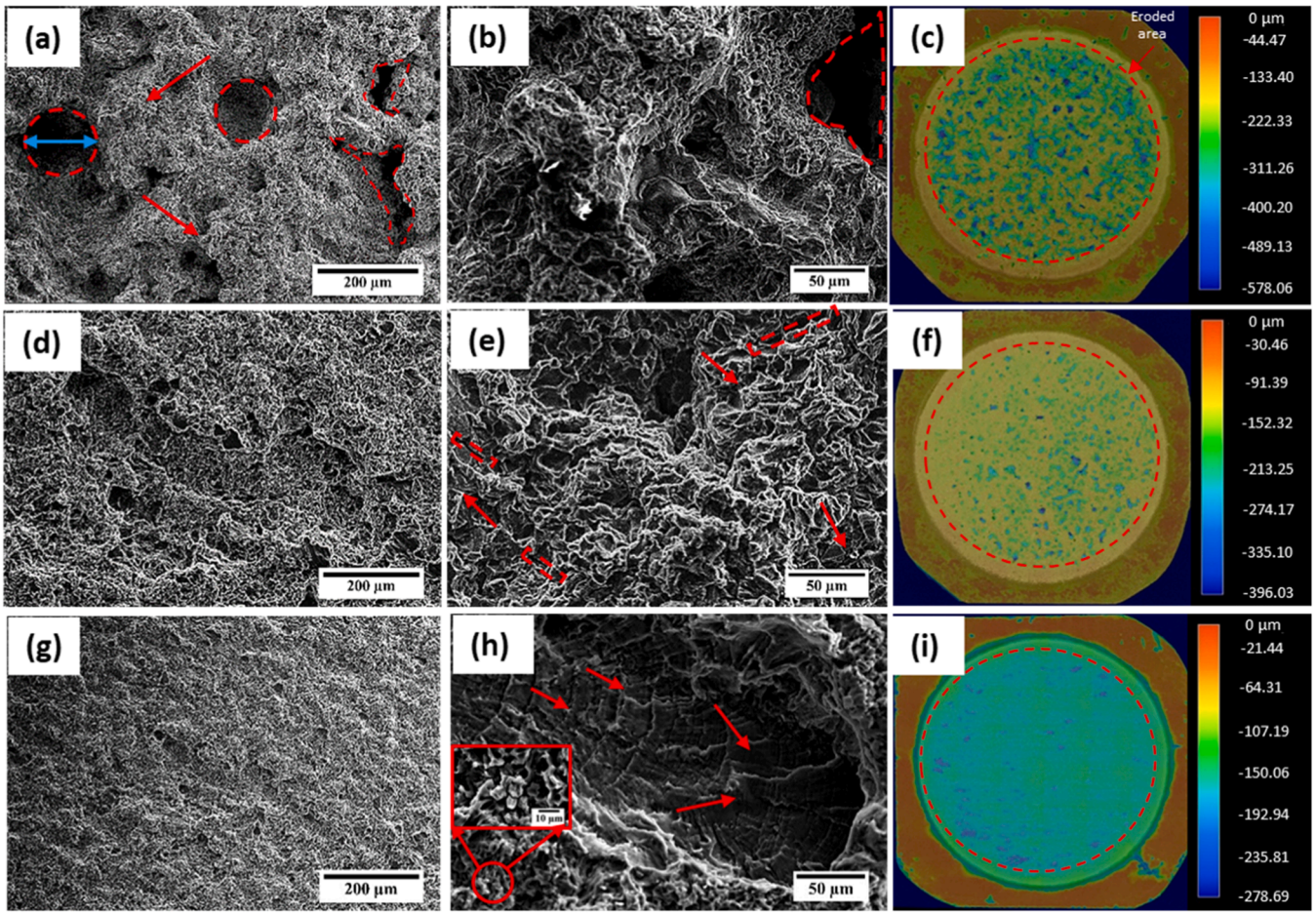

Fig. 9. SEM and 3D scan micrographs, respectively, showing the morphologies of the eroded surface of as-cast alloys A356.2 (a-c), A380 (d-f) and extruded AA6082 (g-i) alloy after 1 h of cavitation exposure at 30 °C. Colour legend depicts a distinct highest (surface) and lowest (depth) point in the image.

to the solid solution hardening effect of Si, Cu, and Zn, which contribute to its high hardness (Table 1). It is worth noting that the specific erosion resistance of the Al cast alloys used in our study was estimated based on the least and most aggressive erosion environments near 20 °C and 30 °C, respectively. In contrast, erosion resistance for alloys not included in our study was estimated solely at ambient temperature conditions (refer to Table A in appendix). Therefore, the comparison in such cases can only be made in terms of exposure time and not temperature. For instance, the erosion response of AA5056 was assessed at 22 °C, while for NAB it was 17 ± 0.5 °C. Thus, it is highly likely that both these alloys will exhibit significantly lower resistance under aggressive erosion conditions near 30 °C. There is even a possibility that A380 and extruded AA6082 may outperform AA5056 and NAB under such conditions making it a more suitable candidate for use in manufacturing critical marine components. It should be noted that this ranking is made solely based on the erosion characteristics (which is the focus of this paper), while other properties such as corrosion resistance should be also taken into account in the materials selection (but this is outside the scope of this study).

In order to gain a comprehensive understanding of the erosion response mechanism, a detailed SEM investigation of the degraded surface was further conducted to analyse the microstructural damage. This analysis aimed at assessing the surface morphology after the ultrasonic erosion tests, quantifying the detrimental effects inflicted by cavitation damage.

3.3. Microstructural damage characterization

The surface morphology of alloy specimen post-cavitation erosion was assessed via SEM and 3D scanning, specifically at the aggressive 30 °C temperature after 60 min of exposure. Morphological images and corresponding 3D height colour maps are presented in Fig. 9, showcasing features like craters, undulations, cracks, and plastic pits across the alloys' surfaces. For instance, Fig. 9a illustrates multiple large craters and undulations in the A356.2 alloy, while Fig. 9d depicts shallow craters and pits in the A380 alloy. In comparison, the extruded AA6082 specimen displayed superior resistance with fewer, smaller pits, and cracks (Fig. 9g), consistent with negligible mass loss (as in Fig. 6c). A closer examination (Fig. 9h) of the impacted surface also revealed distinctive fatigue striations, resembling tire track-like structures, present within the deformed area, a feature not observed in the other alloys. The occurrence of these fatigue striations in the deformed zone of AA6082 can be attributed to the alloy distinct attributes. Unlike A356.2 and A380, which were utilized in their as-cast state, AA6082 is a wrought alloy that underwent heat treatment and extrusion. These processes contribute to improved fatigue strength, toughness, and ductility of the alloy. These enhanced mechanical properties are crucial in countering fatigue-type failure mechanisms, providing an explanation for the presence of fatigue-like striations on the fracture surface of pits in AA6082. This alignment with Vaidya and Reece [36] findings underscores the appearance of such striations particularly in age-hardenable alloys. Although the fundamental erosion mechanism retains conceptual similarity across alloys, individual material attributes, encompassing hardness, ductility, and microstructural characteristics, distinctly shape the extent and rate of material removal [19]. It is important to note here that while visual manifestations of erosion are often observed as pits, craters, undulations, and protrusions on the surface, the primary initiation of cavitation damage occurs along grain boundaries [96]. The localization of erosion is influenced by the intensity of cavitation impacts, where both high and low-intensity impacts cause damage within phases but low-intensity also has the potential to promote grain boundary decohesion. On the other hand, longer exposure times lead to intra-grain cracking. The increased surface roughness is further characterized by the presence of multiple slip and twin bands [37]. The erosion damage in alloys is also related with the probabilistic implosion/impact of bubbles as indicated and explained in Fig. 5(a-f) with microbubble clusters pulsating and imploding repeatedly at specific (favourable) locations, for example, regions exhibiting high porosity in A356.2 (Fig. 2b) thus weakening those regions and eventually initiating damage.

It is well understood that grain size affects the cavitation erosion resistance and the amount of erosion and the implicated damage is influenced by the hardness of the material, which in turn is dictated by the presence of primary and secondary phases within the microstructure. Other than microstructure, the erosion resistance of a material is also dependent on the roughness [97], composition and phase transformations [98]. Among the studied alloys, the A380 and extruded AA6082 alloys exhibited a higher erosion resistance due to the different reasons. In the case of A380, the hard intermetallic particles are relatively uniformly distributed across the area, decreasing the possibility of stress concentration. Additionally, Scheil solidification calculations done for A380 also confirmed that the primary reason behind higher strength and consequently erosion resistance is in fact the solid solution hardening with Cu and Zn content being approximately 1.6 wt% and 3.3 wt%, respectively in Al matrix. The extruded AA6082 alloy, on the contrary, comprises the work-hardened aluminium solid solution arranged in elongated grains, while containing some hard particles albeit in a much smaller quantity (3.2 wt%). The fatigue striations as seen in Fig. 9h may also reflect the ductile nature of damage making the material more suitable to absorb energy and deform plastically delaying the erosion during the initial stages up to 15 min as observed in Fig. 6c. Relatively high erosion of A380 with respect to the extruded AA6082 alloy may be related to the larger grain size and heterogeneous structure that provides many interfaces as shown in Fig. 2(d-f), where the damage can originate. Whereas, the poor erosion resistance of A356.2 is a result of wider areas of relatively soft aluminium solid solution surrounded by brittle intermetallics particles that act as stress concentrators.

The severity of erosion sustained at this aggressive temperature regime was also quantified based on the average crater depth and size obtained from the 3D scan microscopic images. Fig. 10a shows the plot of depths and size (in microns) of formed craters for each alloy at different cavitation exposure period. As it can be seen, for all alloys the crater depth and size increases with the cavitation exposure time. The evolution of crater depth was rather rapid for the A356.2 alloy until 20 min of exposure; in contrast to the A380 and extruded AA6082 alloys where the cavitation was still in its incubation stage. The evolution rate of crater size (equivalent diameter, see double sided arrow in Fig. 9a) was comparatively similar and independent of the cavitation incubation or acceleration stage for all alloys. Overall, the crater depth and size for each alloy increased by approximately 3–6 times and 1–3 times, respectively, after 40 min. In order to find the influence of cavitation on the relative surface damage, we plotted shape factor (defined as the normalised ratio of crater depth to diameter) against cavitation exposure time as shown in Fig. 10b. During initial stages of exposure, the A356.2 alloy exhibited shape factor of almost 40%, about 2–3 times higher than other alloys. Among cast alloys, A380 showed best resistance to surface degradation. It is interesting to see that shape factor increases with erosion time for all alloys except extruded AA6082, for which it showed a decreasing trend. This unique behaviour can be ascribed to the specific combination of mechanical and microstructural properties inherent to AA6082. These inherent characteristics likely played a pivotal role in shaping the erosion pattern evolution over time. While the craters did undergo deepening and expansion, the alloy's inherent mechanical robustness could have induced a distinct alteration in the progression of crater morphology, ultimately leading to the observed decrease in the shape factor. Fig. 10(c-e) shows the representative 3D scan microscopic images of the all the studied alloys, obtained after 60 min of exposure. The large crater dimension observed in case of as-cast A356.2 alloy maybe related to the presence of shrinkage porosity and large equiaxed grains (see Fig. 2b), which provided locations of weakness and vulnerability for erosion initiation. In addition, the heterogeneous distribution of phases and the presence of non-equilibrium eutectics at the dendrite

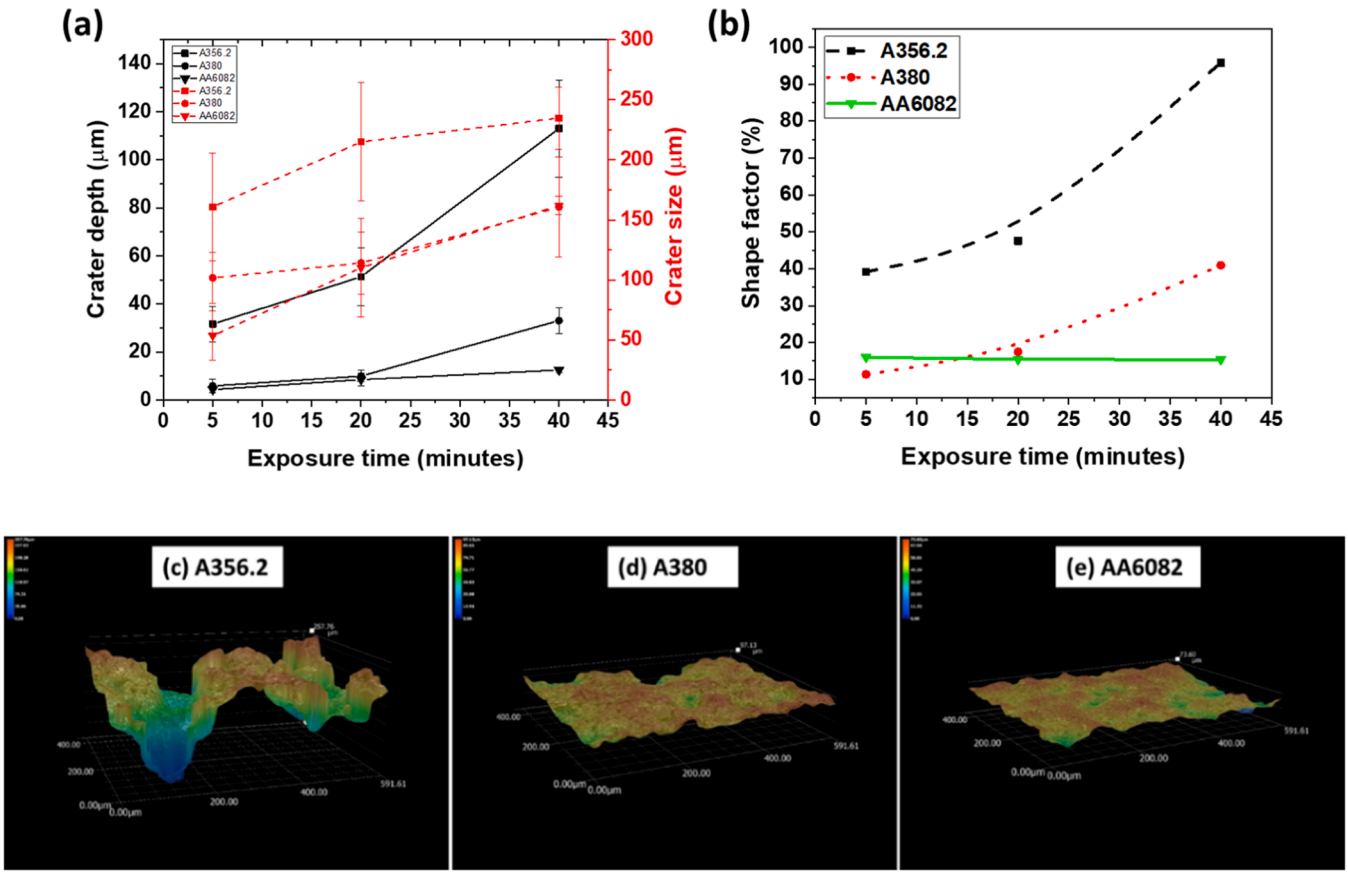

Fig. 10. (a) Evolution of crater showing its mean depth and size of the damaged surface after erosion tests; (b) Normalised shape factor (ratio of crater depth to diameter) as a function of cavitation exposure time for different Al alloys; (c-e) An indicative example showing 3D scan micrographs of the studied Al alloys obtained after 60 min of exposure.

boundaries acted as preferential sites for the formation and violent collapse of cavitation bubbles. With prolonged cavitation exposure, removal of secondary and eutectic phases such as hard and brittle Si particles occurred through rim necking and dislodgment, thereby contributing to the formation of large craters and undulations on the surface [36,99,100].

It should be noted that our experiments were performed in pure water, while many of the marine related applications of interest usually operate in seawater. Salinity of water may have a pronounced effect on cavitation activity (especially due to developed corrosion effects) and to the subsequent erosion damage as recently reported elsewhere [43,101]. Salt addition influences the cavitation process in various ways. Salt crystals in water act as nucleation sites for bubble formation. It has been shown that by introducing salt, gas solubility decreases [102,103], viscosity increases [104], bubble size decreases [105] and coalescence is reduced [106] leading to changes in the cavitation dynamics. Akulichev [107] previously demonstrated that the cavitation threshold diminishes by approximately 10% with specific salt concentrations compared to distilled water. In particular, Francescutto et al. [102] reported that upon moving from distilled water to salt-saturated solutions, parameters such as surface tension, density, viscosity coefficient increase by approximately 12%, 20%, and 70%, respectively, while the gas content decreases by almost one order of magnitude. This interplay between factors contributes to the observed changes in cavitation thresholds. Furthermore, Pflieger et al. [103] observed that the presence of high salt concentrations in the solution leads to a decrease in the average diameter of inertial cavitation bubbles. This underscores the multifaceted nature of cavitation dynamics and its responsiveness to varying environmental conditions. Research by Kozmus et al. [101] reported that as-cast alloys may suffer higher mass loss rate during the incubation period with rates converging in due time irrespective of the test medium (pure or saline water). Nevertheless, the addition of sodium chloride salt led to the increase in size of cavitation zone area by about 1.5 times, which implied a more aggressive environment. While the frequency of bubble collapse remains relatively constant, the mechanical damage caused by the collapse is expected to be similar or even reduced due to developed acoustic shielding effects [101]. Moreover, the phenomenon of bubble coalescence inhibition that occurs upon the introduction of salt in the water makes the nucleation of numerous stable bubble clusters easier but with smaller average size that could potentially, along with the primary cavitation cloud, absorb and shield (cushion) the powerful shock waves and liquid jets that promote the surface damage. From the mechanical effect point of view, the material erosion in saline water should be less severe but may be accelerated through corrosion as recently observed by Zhao et al. [42]. Therefore, further investigation is needed to fully understand and confirm the erosion potential of the studied Al alloys under such environments, which will be the focus of future work in our studies.

4. Conclusions

In this work, the cavitation erosion response of cast Al alloys (A356.2, A380) was evaluated using an ultrasonic transducer under different water temperatures. The results were compared with that of an extruded AA6082 alloy tested under the condition exhibiting maximum surface damage. A comprehensive analysis of the erosion damage on the test specimens was performed and correlated with the acoustic pressure field generated within the cavitation zone measured with the help of hydrophones calibrated in the kHz and MHz range. Results showed that cavitation erosion damage corroborated with the material hardness and

overall microstructure. Among cast alloys, A380 exhibited the best erosion response performing close the extruded AA6082 alloy. Following are the detailed conclusions as obtained from the experimental results:

1. The erosion rate of A356.2 consistently exceeds that of A380 by a significant margin of approximately 2.5–3 times across the temperature range of 10–50 °C.
2. The alloys demonstrates maximum erosion at temperatures around 30 °C, indicating an optimal condition for intensified cavitation activity. Interestingly, this occurs despite the marginally lower acoustic pressure compared to 10 °C. Under this condition, AA6082 displays exceptional erosion resistance, outperforming other tested aluminium alloys.
3. A strong correlation exists between the measured surface roughness and mass loss specifically for the A356.2 alloy across the entire spectrum of erosion stages. However, for the A380 and AA6082, this correlation manifests only after the incubation stage.
4. Detailed microstructure analysis unveil common erosion damage characteristics for all alloys. AA6082, however, exhibits striations within pits indicative of fatigue-type failure.

Thus, among the as-cast alloys, the A380 alloys stands out as an interesting material for manufacturing of geometrically complex components such as pump impellers and propeller blades that can be easily cast in the final shape without need of post processing. The A380 alloy also significantly reduces the cost of production in comparison to wrought alloys that need to be extruded or forged, heat treated and machined into appropriate shapes. However, a complementary erosion-corrosion testing needs to be done to assess the compatibility of A380 with marine environment.

Declaration of Competing Interest

The authors declare that they have no known competing financial interests or personal relationships that could have appeared to influence the work reported in this paper.

Data availability

The raw/processed data required to reproduce these findings are available from the corresponding author on request.

Acknowledgements

This work was financially sponsored by the PAAM (grants EP/W006774/1, EP/W00593X/1 and EP/W006154/1), UltraMelt2 (grants EP/R011001/1, EP/R011095/1 and EP/R011044/1) and EcoUltra2D (grants EP/R031401/1, EP/R031665/1, EP/R031819/1, EP/R031975/1) projects funded by the UK Engineering and Physical Sciences Research Council (EPSRC). Authors greatly acknowledge the help received from Mr. Shazamin Bin Shahrani in SEM imaging, and Dr. Tungky Subroto, Mr. Ian Spacksman and Mr. Radim Asil for selecting and preparing test specimens.

Appendix

Table A
Cavitation erosion performance of different Al based alloys tested in distilled water using ASTM G32 standard.

Materials	Erosion rate (After 1 h of cavitation exposure)	
	µm/h	mg/h
Pure Al	30[93], 68.58[31]	66[108], 30.6[100], 7.2[93]
Pure Al (UST)	–	4.2[41]
AA2024-T351	14.48[31]	2.2[4]
AA2024-T351 (USP)	–	0.8–1.4[4]
A356	–	18[109], 17[89]
A356FA5	–	36[109]
AA5083	3[110], 6[3], 16[90]	40[3]
AA5083 (Anodised)	–	4.7[111]
A5083 (LSPwC)	5[3]	30[3]
AA5083 (LSP)	3.75[3]	22.5[3]
AA5056	–	1.3[6]
AA5056 (MAO)	–	0.5[6]
AA6061-T6	50[91], 60–140[112]	18[91]
AA6061-T651	18.29[31]	–
A6082	9.5[92]	0.75[113], 5[92]
A6082 (Annealed)	–	24.4[114]
A6082 (Age hardened)		16.2[114]
AA6061 (Forged)	–	10.76[89]
AA7075 (MAO)	–	0.5[6]
AA7075 (Anodised)	14[93]	–
AA7075-T651	4.2[115]	–
AlSi7 (UST)	–	10[40]
AlSi7	–	14[40], 37.4[100]
AlSi7-T6 (UST)	–	8[40]
AlSi7-T6	–	8[40], 18.8[100]
Al11Si	–	63.3[100]
AlZn	–	9.3[100]
AlZn-T6	–	7.5[100]
AlZn-T7	–	12.5[100]
Al-Ti (UST)	–	2.7[41]
AlMg (MA)	–	12.6[100]
AlMgLi (MA)	–	8.4[100]
AlSi10Mg	–	7[94]
ASi10Mg-T6	–	6[94]
AlSi10Mg (AM)	–	1[94]

(*continued on next page*)

Table A (*continued*)

Materials	Erosion rate (After 1 h of cavitation exposure)	
	µm/h	mg/h
AlSi10Mg-T6 (AM)	–	7[94]
AlSi10Mg-HIP-T6 (AM)	–	4[94]
AlSi3Cr	–	12.52[89]
AlSi3Cr-T6	–	10.99[89]
AlSi3Mg	–	11[95]
AlSi9Mg	–	5.5[95]
AlSi9CuFe	–	6[95]
AlSi9-T6	–	5[95]
AlSi9CuFe-T6	–	4.5[95]
NAB	0.645[21], 0.662[116]	0.06[43], 0.05[117]

References

[1] R. Simoneau, The optimum protection of hydraulic turbines against cavitation erosion, in: 12th IAHR Symp. Stirling, UK, 1984.

[2] D. Hart, D. Whale, A Review of Cavitation-Erosion Resistance Weld Surfacing Alloys for Hydroturbines, in: 2002.

[3] Tong Z, Jiao J, Zhou W, Yang Y, Chen L, Liu H, Sun Y, Ren X. Improvement in cavitation erosion resistance of AA5083 aluminium alloy by laser shock processing. Surf Coat Technol 2019;377:124799.

[4] Si C, Sun W, Tian Y, Cai J. Cavitation erosion resistance enhancement of the surface modified 2024T351 Al alloy by ultrasonic shot peening. Surf Coat Technol 2023;452:129122.

[5] Corni I, Symonds N. Cavitation erosion performance of steel, ceramics, carbide and PEEK materials. Mater Perform Charact 2018.

[6] Szkodo M, Stanisławska A, Komarov A, Bolewski Ł. Effect of MAO coatings on cavitation erosion and tribological properties of 5056 and 7075 aluminum alloys. Wear 2021;474:203709.

[7] Krella A, Marchewicz A. Effect of mechanical properties of CrN/CrCN coatings and uncoated 1.402 stainless steel on the evolution of degradation and surface roughness in cavitation erosion. Tribol Int 2023;177:107991.

[8] Wang Y, Darut G, Poirier T, Stella J, Liao H, Planche M-P. Ultrasonic cavitation erosion of as-sprayed and laser-remelted yttria stabilized zirconia coatings. J Eur Ceram Soc 2017;37:3623–30.

[9] Liu Z, Khan A, Shen M, Zhu S, Zeng C, Wang F, Fu C. Microstructure and cavitation erosion resistance of arc ion plating NiCrAlY coating on the 304L stainless steel. Tribol Int 2022;173:107618.

[10] Wang Y, Lebon B, Tzanakis I, Zhao Y, Wang K, Stella J, Poirier T, Darut G, Liao H, Planche MP. Experimental and numerical investigation of cavitation-induced erosion in thermal sprayed single splats. Ultrason Sonochem 2019;52:336–43. https://doi.org/10.1016/j.ultsonch.2018.12.008.

[11] Basumatary J, Nie M, Wood RJK. The synergistic effects of cavitation erosion–corrosion in ship propeller materials. J Bio- Tribo-Corros 2015;1:1–12.

[12] Young YL, Motley MR, Barber R, Chae EJ, Garg N. Adaptive composite marine propulsors and turbines: progress and challenges. Appl Mech Rev 2016;68.

[13] T. Yamatogi, H. Murayama, K. Uzawa, K. Kageyama, N. Watanabe, Study on cavitation erosion of composite materials for marine propeller, in: 17th Int. Conf. Compos. Mater. Edinburgh, Scotl., Citeseer, 2009.

[14] Pandit A, Moholkar VS. Bubble behavior in hydrodynamic cavitation: Effect of turbulence. AIChE 1997;43:1641–8.

[15] Tzanakis I, Eskin DG, Georgoulas A, Fytanidis DK. Incubation pit analysis and calculation of the hydrodynamic impact pressure from the implosion of an acoustic cavitation bubble. Ultrason Sonochem 2014;21:866–78. https://doi.org/10.1016/j.ultsonch.2013.10.003.

[16] Vyas B, Preece CM. Stress produced in a solid by cavitation. J Appl Phys 2008;47:5133. https://doi.org/10.1063/1.322584.

[17] Yusvika M, Prabowo AR, Tjahjana DDDP, Sohn JM. Cavitation Prediction of Ship Propeller Based on Temperature and Fluid Properties of Water. J Mar Sci Eng 2020;8:465. https://doi.org/10.3390/jmse8060465.

[18] Tzanakis I, Hadfield M, Garland N. Cavitation damage incubation with typical fluids applied to a scroll expander system. Tribol Int 2011;44:1668–78. https://doi.org/10.1016/j.triboint.2011.06.013.

[19] Tzanakis I, Bolzoni L, Eskin DG, Hadfield M. Evaluation of cavitation erosion behavior of commercial steel grades used in the design of fluid machinery. Metall Mater Trans A Phys Metall Mater Sci 2017;48:2193–206. https://doi.org/10.1007/s11661-017-4004-2.

[20] Tzanakis I, Georgoulas A, Hadfield M, Kotsovinos N. Cavitation erosion behaviour of the steel plate of a scroll expander system. WIT Trans Eng Sci 2012;76:129–37. https://doi.org/10.2495/td120111.

[21] Basumatary J. Cavitation Erosion-corrosion of Ship Propeller Materials. ASTM International,; 2017. https://doi.org/10.1520/stp156320120148.

[22] Tzanakis I, Hadfield M, Georgoulas A, Kotsovinos N. Cavitation damage observations within scrollexpander lubrication systems. WIT Trans Eng Sci 2010;66:261–72. https://doi.org/10.2495/td100221.

[23] Tzanakis I, Hadfield M, Henshaw I. Observations of acoustically generated cavitation bubbles within typical fluids applied to a scroll expander lubrication system. Exp Therm Fluid Sci 2011;35:1544–54. https://doi.org/10.1016/j.expthermflusci.2011.07.005.

[24] Tzanakis I, Georgoulas A, Hadfield M, Kotsovinos N. Cavitation erosion damage of scroll steel plates by high-speed gas working fluid. Int J Comput Methods Exp Meas 2014;2:168–83. https://doi.org/10.2495/CMEM-V2-N2-168-183.

[25] Ylönen M, Saarenrinne P, Miettinen J, Franc JP, Fivel M, Nyyssönen T. Cavitation erosion resistance assessment and comparison of three francis turbine runner materials. Mater Perform Charact 2018;7. https://doi.org/10.1520/mpc20180015.

[26] Syahid M, Sofyan BT, Mukhlisa I. Microstructure and mechanical properties of Al-10Zn-4.5Mg-xCu turbine impeller produced by investmen. Int J Smart Mater Mechatron 2016;2:18–21. https://doi.org/10.20342/IJSMM.2.1.21.

[27] Syahid M, Sofyan BT, Basuki SG, Adam B. Characterization of Al-7Si-Mg-Cu turbine impeller produced by investment casting. Adv Mater Res 2013;789:324–9. https://doi.org/10.4028/WWW.SCIENTIFIC.NET/AMR.789.324.

[28] Lloyd GS. Materials for propeller fabrication. In: Rules Classif. Constr. Mater. Weld.. 2nd ed..,. Hamburg: Germanischer Lloyd Aktiengesellschaft; 2009. p. 1–11. www.gl-group.com (accessed May 23, 2022).

[29] Vardhan DH, Ramesh A, Reddy BCM. A review on materials used for marine propellers. Mater Today Proc 2019;18:4482–90. https://doi.org/10.1016/j.matpr.2019.07.418.

[30] Welty GD, Davis LW. Light alloy propeller blades. J Aeronaut Sci 1935;2:35–8. https://doi.org/10.2514/8.66.

[31] Richman RH, McNaughton WP. Correlation of cavitation erosion behavior with mechanical properties of metals. Wear 1990;140:63–82. https://doi.org/10.1016/0043-1648(90)90122-Q.

[32] Vyas B, Preece CM. Cavitation-induced deformation of aluminum. In: Erosion, Wear, Interfaces with Corros. ASTM International; 1974. p. 77–105.

[33] Hansson I, Morch KA. The initial stage of cavitation erosion on aluminium in water flow. J Phys D Appl Phys 1978;11:147. https://doi.org/10.1088/0022-3727/11/2/012.

[34] Hammitt FG, De MK. Cavitation erosion of aluminum considering bubble collapse, pulse height spectra and cavitation erosion efficiency. Wear 1979;55:221–34. https://doi.org/10.1016/0043-1648(79)90154-6.

[35] Priyadarshi A, Khavari M, Bin Shahrani S, Subroto T, Yusuf LA, Conte M, et al. In-situ observations and acoustic measurements upon fragmentation of free-floating intermetallics under ultrasonic cavitation in water. Ultrason Sonochem 2021;80:105820. https://doi.org/10.1016/j.ultsonch.2021.105820.

[36] Vaidya S, Preece CM. Cavitation erosion of age-hardenable aluminum alloys. 1978 93 Metall Trans A 1978;9:299–307. https://doi.org/10.1007/BF02646379.

[37] Rao BCS, Buckley DH. Deformation and erosion of F.C.C. metals and alloys under cavitation attack. Mater Sci Eng 1984;67:55–67. https://doi.org/10.1016/0025-5416(84)90031-4.

[38] Rao BCS, Buckley DH. Erosion of aluminum 6061-T6 under cavitation attack in mineral oil and water. Wear 1985;105:171–82. https://doi.org/10.1016/0043-1648(85)90023-7.

[39] Lee SJ, Kim KH, Kim SJ. Surface analysis of Al-Mg alloy series for ship after cavitation test. Surf Interface Anal 2012;44:1389–92. https://doi.org/10.1002/sia.4953.

[40] Pola A, Montesano L, Tocci M, La Vecchia GM. Influence of Ultrasound Treatment on Cavitation Erosion Resistance of AlSi7 Alloy. Mater (Basel) 2017;10. https://doi.org/10.3390/ma10030256.

[41] Zhao J, Jiang Z, Zhu J, Zhang J, Li Y. Investigation on ultrasonic cavitation erosion behaviors of Al and Al-5Ti alloys in the distilled water. Met (Basel) 2020;10:1631. https://doi.org/10.3390/met10121631.

[42] Zhao J, Ning L, Zhu J, Li Y, Brutti S, Kharton VV, et al. Investigation on ultrasonic cavitation erosion of aluminum–titanium alloys in sodium chloride solution. Crystals 2021;11:1299. https://doi.org/10.3390/cryst11111299.

[43] Li Y, Lian Y, Sun Y. Comparison of cavitation erosion behaviors between the as-cast and friction stir processed Ni–Al bronze in distilled water and artificial seawater. J Mater Res Technol 2021;13:906–18. https://doi.org/10.1016/j.jmrt.2021.05.015.

[44] Plesset MS. Temperature effects in cavitation damage. J Basic Eng 1972;94:559–63. https://doi.org/10.1115/1.3425484.

[45] Peng K, Qin FGF, Jiang R, Kang S. Interpreting the influence of liquid temperature on cavitation collapse intensity through bubble dynamic analysis. Ultrason Sonochem 2020;69:105253. https://doi.org/10.1016/j.ultsonch.2020.105253.

[46] Yu-Kang Z, Hammitt FG. Cavitation erosion incubation period. Wear 1983;86: 299–313. https://doi.org/10.1016/0043-1648(83)90168-0.

[47] Hattori S, Goto Y, Fukuyama T. Influence of temperature on erosion by a cavitating liquid jet. Wear 2006;260:1217–23. https://doi.org/10.1016/j.wear.2005.08.001.

[48] Dular M. Hydrodynamic cavitation damage in water at elevated temperatures. Wear 2016;346–347:78–86. https://doi.org/10.1016/j.wear.2015.11.007.

[49] Hosbach M, Sander T, Leuteritz U, Pfitzner M. Temperature and Pressure Effects on Cavitation Erosion in Diesel-Like Fuels. In: Proc. 10th Int. Symp. Cavitation. ASME Press; 2018. p. 978–83. https://doi.org/10.1115/1.861851_ch187.

[50] D.B. Preso, X. Peng, Y. Cao, M. Farhat, Temperature effect on erosion due to high-speed cavitating jet, in: 11th Int. Sumpos. Cavitation, Daejon, 2009: pp. 1–4.

[51] Morton JA, Eskin DG, Grobert N, Mi J, Porfyrakis K, Prentice P, Tzanakis I. Effect of temperature and acoustic pressure during ultrasound liquid-phase processing of graphite in water. JOM 2021;73:3745–52. https://doi.org/10.1007/S11837-021-04910-9/TABLES/1.

[52] Standard Test Method for Cavitation Erosion Using Vibratory Apparatus (ASTM G32), in: Annu. B. ASTM Stand. 20, n.d. ⟨https://www.astm.org/g0032–16r21e01.html⟩ (accessed August 31, 2022).

[53] Khavari M, Priyadarshi A, Subroto T, Beckwith C, Pericleous K, Eskin DG, Tzanakis I. Scale up design study on process vessel dimensions for ultrasonic processing of water and liquid aluminium. Ultrason Sonochem 2021;76:105647. https://doi.org/10.1016/j.ultsonch.2021.105647.

[54] Khavari M, Priyadarshi A, Hurrell A, Pericleous K, Eskin D, Tzanakis I. Characterization of shock waves in power ultrasound. J Fluid Mech 2021;915:R3. https://doi.org/10.1017/jfm.2021.186.

[55] Chahine GL, Franc JP, Karimi A. Cavitation and cavitation erosion. In: Adv. Exp. Numer. Tech. Cavitation Eros. Predict. Kluwer Academic Publishers; 2014. p. 3–20. https://doi.org/10.1007/978-94-017-8539-6_1/COVER.

[56] van Iersel MM, Benes NE, Keurentjes JTF. Importance of acoustic shielding in sonochemistry. Ultrason Sonochem 2008;15:294–300. https://doi.org/10.1016/j.ultsonch.2007.09.015.

[57] Khavari M, Priyadarshi A, Morton J, Porfyrakis K, Pericleous K, Eskin D, Tzanakis I. Cavitation-induced shock wave behaviour in different liquids. Ultrason Sonochem 2023;94:106328. https://doi.org/10.1016/j.ultsonch.2023.106328.

[58] Tzanakis I, Lebon GSB, Eskin DG, Pericleous KA. Characterizing the cavitation development and acoustic spectrum in various liquids. Ultrason Sonochem 2017; 34:651–62. https://doi.org/10.1016/j.ultsonch.2016.06.034.

[59] Fuchs FJ. Ultrasonic cleaning and washing of surfaces. Power Ultrason Appl High-Intensity Ultrasound 2015:577–609. https://doi.org/10.1016/B978-1-78242-028-6.00019-3.

[60] Young SG, Johnston JR. Effect of Temperature and Pressure on Cavitation Damage in Sodium. ASTM International,; 1970.

[61] Hammitt FG, Rogers DO. Effects of pressure and temperature variation in vibratory cavitation damage test. J Mech Eng Sci 1970;12:432–9.

[62] El Hassan M, Bukharin N, Al-Kouz W, Zhang JW, Li WF. A review on the erosion mechanism in cavitating jets and their industrial applications. Appl Sci 2021;11: 3166. https://doi.org/10.3390/app11073166.

[63] Nagalingam AP, Yeo SH. Effects of ambient pressure and fluid temperature in ultrasonic cavitation machining. Int J Adv Manuf Technol 2018;98:2883–94. https://doi.org/10.1007/s00170-018-2481-0.

[64] Mori Y, Hijikata K, Nagatani T. Effect of dissolved gas on bubble nucleation. Int J Heat Mass Transf 1976;19:1153–9. https://doi.org/10.1016/0017-9310(76)90149-6.

[65] Kwak HY, Oh SD. Gas–vapor bubble nucleation—a unified approach. J Colloid Interface Sci 2004;278:436–46. https://doi.org/10.1016/j.jcis.2004.06.020.

[66] Apfel RE. The role of impurities in cavitation-threshold determination. J Acoust Soc Am 1970;48:1179–86. https://doi.org/10.1121/1.1912258.

[67] Morton JA, Khavari M, Qin L, Maciejewska BM, Tyurnina AV, Grobert N, et al. New insights into sono-exfoliation mechanisms of graphite: In situ high-speed imaging studies and acoustic measurements. Mater Today 2021;49:10–22. https://doi.org/10.1016/j.mattod.2021.05.005.

[68] Rooze J, Rebrov EV, Schouten JC, Keurentjes JTF. Dissolved gas and ultrasonic cavitation – A review. Ultrason Sonochem 2013;20:1–11. https://doi.org/10.1016/j.ultsonch.2012.04.013.

[69] Kaur A, Morton JA, Tyurnina AV, Priyadarshi A, Holland A, Mi J, et al. Temperature as a key parameter for graphene sono-exfoliation in water. Ultrason Sonochem 2022;90:106187. https://doi.org/10.1016/J.ultsonch.2022.106187.

[70] Kim T-H, Kim H-Y. Disruptive bubble behaviour leading to microstructure damage in an ultrasonic field. J Fluid Mech 2014;750:355–71. https://doi.org/10.1017/jfm.2014.267.

[71] Jayaprakash A, Choi JK, Chahine GL, Martin F, Donnelly M, Franc JP, et al. Scaling study of cavitation pitting from cavitating jets and ultrasonic horns. Wear 2012;296:619–29. https://doi.org/10.1016/j.wear.2012.07.025.

[72] Plesset MS, Chapman RB. Collapse of an initially spherical vapour cavity in the neighbourhood of a solid boundary. J Fluid Mech 1971;47:283–90. https://doi.org/10.1017/S0022112071001058.

[73] Yusuf L, Symes MD, Prentice P. Characterising the cavitation activity generated by an ultrasonic horn at varying tip-vibration amplitudes. Ultrason Sonochem 2021;70:105273. https://doi.org/10.1016/j.ultsonch.2020.105273.

[74] Priyadarshi A, Khavari M, Subroto T, Prentice P, Pericleous K, Eskin D, et al. Mechanisms of ultrasonic de-agglomeration of oxides through in-situ high-speed observations and acoustic measurements. Ultrason Sonochem 2021;79:105792. https://doi.org/10.1016/j.ultsonch.2021.105792.

[75] Jian W, Petkovšek M, Houlin L, Širok B, Dular M. Combined numerical and experimental investigation of the cavitation erosion process. J Fluids Eng Trans Asme 2015;137. https://doi.org/10.1115/1.4029533/382248.

[76] Ohl CD, Ikink R. Shock-wave-induced jetting of micron-size bubbles. Phys Rev Lett 2003;90:4. https://doi.org/10.1103/PhysRevLett.90.214502.

[77] Ogloblina D, Schmidt SJ, Adams NA. Simulation and analysis of collapsing vapor-bubble clusters with special emphasis on potentially erosive impact loads at walls. In: EPJ Web Conf. EDP Sciences; 2018. p. 02079. https://doi.org/10.1051/epjconf/201818002079.

[78] Bena T, Bordeasu I, Craciunescu CM. Relationships between microstructure, roughness parameters and ultrasonic cavitation erosion behaviour of nodular cast iron, EN-GJS-400-15. Rev Chim 2018;69:612–7.

[79] Bena T, Mitelea I, Bordeau I, Crăciunescu CM. Roughness parameters during cavitation exposure of nodular cast iron with ferrite-pearlite microstructure. IOP Conf Ser Mater Sci Eng 2018;416:012011. https://doi.org/10.1088/1757-899X/416/1/012011.

[80] Wang L, Mao J, Xue C, Ge H, Dong G, Zhang Q, et al. Cavitation-erosion behavior of laser cladded low-carbon cobalt-based alloys on 17-4PH stainless steel. Opt Laser Technol 2023;158:108761. https://doi.org/10.1016/j.optlastec.2022.108761.

[81] Szala M, Chocyk D, Skic A, Kamiński M, Macek W, Turek M. Effect of Nitrogen Ion Implantation on the Cavitation Erosion Resistance and Cobalt-Based Solid Solution Phase Transformations of HIPed Stellite 6. Mater (Basel) 2021;14:2324. https://doi.org/10.3390/ma14092324.

[82] Krella AK. Degradation and protection of materials from cavitation erosion: a review. Mater (Basel) 2023;16:2058. https://doi.org/10.3390/ma16052058.

[83] Hucińska J, Glowacka M. Cavitation erosion of copper and copper-based alloys. Metall Mater Trans A Phys Metall Mater Sci 2001;32:1325–33. https://doi.org/10.1007/S11661-001-0223-6.

[84] Chiu KY, Cheng FT, Man HC. Evolution of surface roughness of some metallic materials in cavitation erosion. Ultrasonics 2005;43:713–6.

[85] Patella RF, Reboud J-L, Archer A. Cavitation damage measurement by 3D laser profilometry. Wear 2000;246:59–67.

[86] Hattori S, Kitagawa T. Analysis of cavitation erosion resistance of cast iron and nonferrous metals based on database and comparison with carbon steel data. Wear 2010;269:443–8. https://doi.org/10.1016/j.wear.2010.04.031.

[87] Zakrzewska DE, Krella AK. Cavitation erosion resistance influence of material properties. Adv Mater Sci 2019;19:18–34. https://doi.org/10.2478/adms-2019-0019.

[88] Hattori S, Nakao E. Cavitation erosion mechanisms and quantitative evaluation based on erosion particles. Wear 2001;249:839–45.

[89] Gottardi G, Tocci M, Montesano L, Pola A. Cavitation erosion behaviour of an innovative aluminium alloy for Hybrid Aluminium Forging. Wear 2018;394–395: 1–10. https://doi.org/10.1016/j.wear.2017.10.009.

[90] Istrate D, Sbârcea B-G, Demian AM, Buzatu AD, Salcianu L, Bordeasu I, et al. Correlation between Mechanical Properties-Structural Characteristics and Cavitation Resistance of Cast Aluminum Alloy Type 5083. Crystals 2022;12:1538. https://doi.org/10.3390/cryst12111538.

[91] B.C.S. Rao, D.H. Buckley, D.H. Buckley, Cavitation pitting and erosion of aluminum 6061-T6 in mineral oil water, Houston, 1983.

[92] Ibanez I, Zeqiri B, Hodnett M, Frota MN. Cavitation-erosion measurements on engineering materials. Eng Sci Technol Int J 2020;23:1486–98. https://doi.org/10.1016/j.jestch.2020.06.001.

[93] Choi JK, Jayaprakash A, Chahine GL. Scaling of cavitation erosion progression with cavitation intensity and cavitation source. Wear 2012;278–279:53–61. https://doi.org/10.1016/j.wear.2012.01.008.

[94] Girelli L, Tocci M, Montesano L, Gelfi M, Pola A. Investigation of cavitation erosion resistance of AlSi10Mg alloy for additive manufacturing. Wear 2018; 402–403:124–36. https://doi.org/10.1016/j.wear.2018.02.018.

[95] Tocci M, Pola A, Montesano L, La Vecchia GM. Evaluation of cavitation erosion resistance of Al-Si casting alloys: effect of eutectic and intermetallic phases. Frat Ed Integrità Strutt 2018;12:218–30. https://doi.org/10.3221/IGF-ESIS.43.17.

[96] Karimi A, Avellan F. Comparison of erosion mechanisms in different types of cavitation. Wear 1986;113:305–22. https://doi.org/10.1016/0043-1648(86)90031-1.

[97] Lin J, Wang Z, Cheng J, Kang M, Fu X, Hong S. Effect of Initial Surface Roughness on Cavitation Erosion Resistance of Arc-Sprayed Fe-Based Amorphous/Nanocrystalline Coatings. Coatings 2017;7:200. https://doi.org/10.3390/coatings7110200.

[98] Xiaojun Z, Procopiak LAJ, Souza NC, D'oliveira ASCM. Phase transformation during cavitation erosion of a Co stainless steel. Mater Sci Eng A 2003;358: 199–204. https://doi.org/10.1016/S0921-5093(03)00297-1.

[99] Vyas B, Preece CM. Cavitation erosion of face centered cubic metals. Metall Trans A 1977;8:915–23. https://doi.org/10.1007/BF02661573.

[100] Tomlinson WJ, Matthews SJ. Cavitation erosion of aluminium alloys. J Mater Sci 1994;29:1101–8.

[101] Kozmus G, Zevnik J, Hočevar M, Dular M, Petkovšek M. Characterization of cavitation under ultrasonic horn tip – Proposition of an acoustic cavitation parameter. Ultrason Sonochem 2022;89:106159. https://doi.org/10.1016/j.ultsonch.2022.106159.

[102] Francescutto A, Iernetti G, Ciuti P, Carpenedo L, Dezhkunov NV. Acoustic cavitation thresholds in NaCl-water solutions. La Houille Blanc 1992;47:535–8. https://doi.org/10.1051/LHB/1992053.

[103] Pflieger R, Nikitenko SI, Ashokkumar M. Effect of NaCl salt on sonochemistry and sonoluminescence in aqueous solutions. Ultrason Sonochem 2019;59:104753. https://doi.org/10.1016/j.ultsonch.2019.104753.
[104] Goncalves FA, Kestin J. The Viscosity of NaCl and KCl Solutions in the Range 25–50°C. Ber Der Bunsenges Für Phys Chem 1977;81:1156–61. https://doi.org/10.1002/BBPC.19770811108.
[105] Brotchie A, Statham T, Zhou M, Dharmarathne L, Grieser F, Ashokkumar M. Acoustic bubble sizes, coalescence, and sonochemical activity in aqueous electrolyte solutions saturated with different gases. Langmuir 2010;26:12690–5. https://doi.org/10.1021/LA1017104/SUPPL_FILE/LA1017104_SI_001.PDF.
[106] Weissenborn PK, Pugh RJ. Surface Tension and Bubble Coalescence Phenomena of Aqueous Solutions of Electrolytes. Langmuir 1995;11:1422–6. https://doi.org/10.1021/LA00005A002/ASSET/LA00005A002.FP.PNG_V03.
[107] Akulichev VA. Hydration of ions and the cavitation resistance of water. Sov Phys Acoust 1966;12:144–50.
[108] Opare W, Kang C, Wei X, Liu H, Wang H. Comparative investigation of ultrasonic cavitation erosion for three materials in deionized water. Proc Inst Mech Eng Part J J Eng Tribol 2020;234:1425–35. https://doi.org/10.1177/1350650119899547/ASSET/IMAGES/LARGE/10.1177_1350650119899547-FIG2.JPEG.
[109] Maksimović VM, Devečerski AB, Došen A, Bobić I, Erić MD, Volkov-Husović T. Comparative Study on Cavitation Erosion Resistance of A356 Alloy and A356FA5 Composite. Trans Indian Inst Met 2016;70:97–105. https://doi.org/10.1007/S12666-016-0864-1.
[110] Istrate D, Ghera C, Sălcianu L, BORDEAŞU I, GHIBAN B, Băzăvan DV, Micu LM, STROIŢĂ D-C, Ostoia D. Heat Treatment Influence of Alloy 5083 on Cavitational Erosion Resistance.. Hidraulica,; 2021.
[111] Fahim J, Hadavi SMM, Ghayour H, Hassanzadeh Tabrizi SA. Cavitation erosion behavior of super-hydrophobic coatings on Al5083 marine aluminum alloy. Wear 2019;424–425:122–32. https://doi.org/10.1016/j.wear.2019.02.017.
[112] Caccese V, Light KH, Berube KA. Cavitation erosion resistance of various material systems. Ships Offshore Struct 2010;1:309–22. https://doi.org/10.1533/saos.2006.0136.
[113] Laguna-Camacho JR, Lewis R, Vite-Torres M, Méndez-Méndez JV. A study of cavitation erosion on engineering materials. Wear 2013;301:467–76. https://doi.org/10.1016/j.wear.2012.11.026.
[114] Franț F, Mitelea I, Bordeaşu I, Codrean C, Mutaşcu D. Effect of some heat treatments on cavitation erosion resistance of the EN AW - 6082 alloy. In: Met. 2019 - 28th Int. Conf. Metall. Mater. TANGER Ltd; 2019. p. 663–7. https://doi.org/10.37904/metal.2019.835.
[115] Bordeasu I, Luca AN, Lazar I, Lazar D, Badarau R, Ghiban B, Bazatu AD, Demian AM, Odagiu OP, Micu LM. Modification of Cavitation Erosion Resistance of Aluminum Alloy 7075 by Maintaining of Artificial Aging Heat Treatment at 180°C. Hidraulica,; 2022. ⟨https://hidraulica.fluidas.ro/2022/nr4/33-41.pdf⟩ (accessed January 10, 2023).
[116] K.J. KarisAllen, C.A. Taweel, Evaluation of Cavitation Erosion Behavior of a Laser Surface Melted Experimental Nickel Aluminum Bronze, Defence Research Establishment Atlantic, Halifax, Nova Scotia, 1997.
[117] Li Y, Lian Y, Sun Y. Cavitation erosion behavior of friction stir processed nickel aluminum bronze. J Alloy Compd 2019;795:233–40. https://doi.org/10.1016/j.jallcom.2019.04.302.